AGU PUBLICATIONS

Geochemistry, Geophysics, Geosystems

RESEARCH ARTICLE
10.1002/2017GC007309

Crystallographic Preferred Orientation of Olivine in Sheared Partially Molten Rocks: The Source of the "a-c Switch"

Chao Qi[1], Lars N. Hansen[2], David Wallis[2], Benjamin K. Holtzman[3], and David L. Kohlstedt[1]

[1]Department of Earth Sciences, University of Minnesota, Minneapolis, MN, USA, [2]Department of Earth Sciences, University of Oxford, Oxford, UK, [3]Lamont Doherty Earth Observatory, Columbia University, Palisades, NY, USA

Key Points:
- A CPO of olivine with girdles of [100] and [001] axes in the shear plane occurs in sheared partially molten mantle rocks
- This observed CPO is weak, exhibits little change with strain and stress, and induces different seismic anisotropy from melt-free olivine
- We proposed a model consisting of two mechanisms for CPO formation to explain the occurrence and evolution of the observed CPO

Supporting Information:
- Supporting Information S1
- Figure S1
- Figure S2

Correspondence to:
C. Qi,
qixxx063@umn.edu

Citation:
Qi, C., Hansen, L. N., Wallis, D., Holtzman, B. K., & Kohlstedt, D. L. (2018). Crystallographic preferred orientation of olivine in sheared partially molten rocks: The source of the "a-c switch". *Geochemistry, Geophysics, Geosystems*, *19*, 316–336. https://doi.org/10.1002/2017GC007309

Received 30 OCT 2017
Accepted 27 DEC 2017
Accepted article online 17 JAN 2018
Published online 2 FEB 2018

Abstract To investigate the mechanism that produces the crystallographic preferred orientations (CPO) characteristic of sheared partially molten rocks of mantle composition, we analyzed the microstructures of samples of olivine plus 7% basaltic melt deformed in torsion to shear strains as large as $\gamma = 13.3$. Electron backscattered diffraction (EBSD) observations reveal a CPO characterized by a weak a-c girdle in the shear plane that develops by $\gamma \approx 4$. This CPO, which exhibits a slightly stronger alignment of [001] than [100] axes in the shear direction, changes little in both strength and distribution with increasing stress and with increasing strain. Furthermore, it is significantly weaker than the CPO observed for dry, melt-free olivine aggregates. Orientation maps correlated with grain shape measurements from tangential, radial, and transverse sections indicate that olivine grains are longer along [001] axes than along [100] axes and shortest along [010] axes. This morphology is similar to that of olivine grains in a mafic melt. We conclude that the weak a-c girdle observed in sheared partially molten rocks reflects contributions from two processes. Due to their shape-preferred orientation (SPO), grains rotate to align their [001] axes parallel to the flow direction. At the same time, dislocation glide on the (010)[100] slip system rotates [100] axes into the flow direction. The presence of this CPO in partially molten regions of the upper mantle significantly impacts the interpretation of seismic anisotropy and kinematics of flow.

1. Introduction

Shear deformation of partially molten, olivine-rich aggregates at modest confining pressures produces a crystallographic preferred orientation (CPO) distinctly different from that obtained in similar laboratory experiments on melt-free samples. In the latter, [100] axes strongly align approximately parallel to the shear direction with [010] axes nearly perpendicular to the shear plane, as illustrated in Figure 1a. This CPO suggests a dominant role of glide on (010)[100] (Phakey et al., 1972), the weakest slip system in olivine under modest-pressure, high-temperature, anhydrous conditions (Bai et al., 1991; Durham & Goetze, 1977; Ricoult & Kohlstedt, 1985). In contrast, in sheared melt-bearing samples, while [010] axes still strongly align nearly perpendicular to the shear plane, [100] and [001] axes form a weak girdle in the shear plane with a slight preference for [001] in the shear direction (sometimes referred to as AG-type, Mainprice, 2007), as sketched in Figure 1b. This change in the CPO observed for melt-free samples to that obtained for melt-bearing samples constitutes the "a-c switch" first documented by Holtzman et al. (2003a).

The simplest explanation or the null hypothesis for the formation of this weak, girdled CPO involves deformation on both the (010)[100] and the (010)[001] slip system with a slightly greater contribution from the latter to the total strain. This explanation, however, conflicts with results from measurements of creep properties of olivine single crystals, which demonstrate that the (010)[001] slip system deforms almost a factor of 10^3 more slowly than the (010)[100] slip system under identical thermomechanical conditions (Durham & Goetze, 1977). Possible changes in chemical environment, such as silica activity associated with the presence of melt, produce only a very modest change in the relative strengths of these two slip systems (Bai et al., 1991; Ricoult & Kohlstedt, 1985). Furthermore, the fabric expected for deformation dominated by the (010)[001] slip system, which is illustrated in Figure 1c, primarily develops at high stresses under hydrous conditions (Jung & Karato, 2001) and at very high pressures under anhydrous conditions (Couvy et al., 2004; Ohuchi et al., 2011; Raterron et al., 2009), not those explored in the present study.

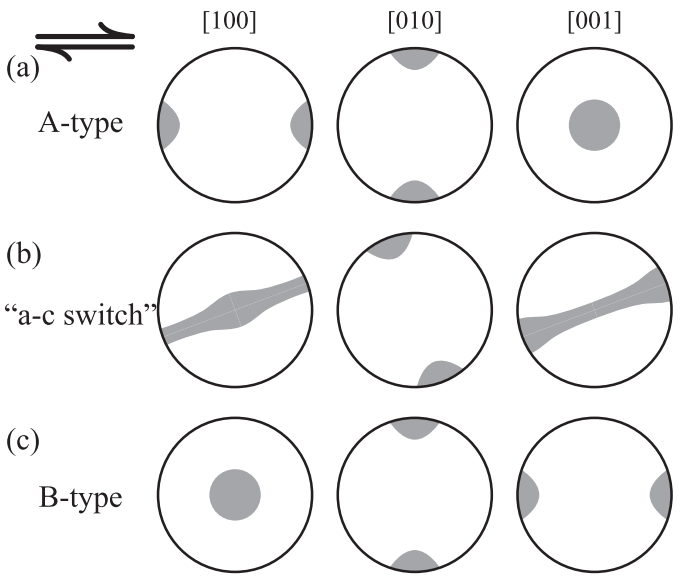

Figure 1. Schematic drawings of (a) A-type, (b) "a-c switch," and (c) B-type crystallographic fabrics. Pole figures are shown for each of the three principal crystallographic axes. Gray regions denote the dominant orientations of grains. The sense of shear is top to the right.

An alternative hypothesis for the a-c switch (Holtzman et al., 2003b; Kohlstedt & Holtzman, 2009) emphasized the importance of stress-induced anisotropy in melt distribution in partially molten rocks observed in experiments (Bussod & Christi, 1991; Daines & Kohlstedt, 1997; Kohlstedt & Zimmerman, 1996; Takei, 2001; Zimmerman et al., 1999). For grain boundaries normal to the least compressive stress in partially molten samples of an olivine-basalt analog stressed in uniform pure shear, the fraction of grain boundary area replaced by melt increased relative to that in an unstressed sample (Takei, 2001). This behavior also occurs in samples of olivine plus basalt deformed in torsional shear to low strains (M. Peč, personal communication, 2017). At high shear strains ($\gamma > 1$), this melt preferred orientation (MPO) rotates from 45° to 15–25° to the shear plane, still antithetic to the shear direction (Holtzman et al., 2003b; King et al., 2010; Kohlstedt & Zimmerman, 1996; Zimmerman et al., 1999). Based on these observations, it was proposed that the a-c switch occurred because melt alignment causes strain to partition between deformation mechanisms (diffusion creep, dislocation-accommodated grain boundary sliding, and dislocation creep) in an anisotropic manner such that the relative contribution of each mechanism depends on direction in the sample. In this conceptual model, deformation in the shear plane in the shear direction is preferentially accommodated by melt-assisted grain-boundary diffusion creep (Cooper & Kohlstedt, 1986), reducing the need for dislocation glide to accommodate deformation and thus reducing *a* axis alignment in the shear direction. This anisotropy in the relative contributions of various deformation mechanisms to strain is possible if deformation occurs near the boundary between dislocation-accommodated grain boundary sliding and diffusion creep (de Bresser et al., 2001; Hansen et al., 2011; Hirth & Kohlstedt, 2003; Kohlstedt & Hansen, 2015).

In the present paper, we propose a new hypothesis for inducing the a-c switch based on detailed microstructural analyses of samples of olivine + basalt deformed to high strain. Our proposed mechanism involves contributions from shape-controlled grain rotation of elongated olivine grains (e.g., Miyazaki et al., 2013) and from crystal plasticity (e.g., Zhang & Karato, 1995), both coupled with grain-boundary sliding (GBS). Grains in our partially molten samples exhibit a clear shape-preferred orientation (SPO), with the longest axes along [001] and shortest axes along [010]. This morphology is similar to that of olivine grains in an ultramafic melt (e.g., Fleet, 1975; Schwindinger & Anderson, 1989; t'Hart, 1978). The CPO observed in sheared partially molten olivine-basalt aggregates then develops by alignment of the long axis in the flow field combined with dislocation glide on the (010)[100] slip system.

2. Methods

2.1. Sample Preparation and Deformation Experiments

Samples were fabricated from mixtures of fine-grained powders of olivine and 10 vol % either mid-ocean ridge basalt (MORB) (Cooper & Kohlstedt, 1984) or Hawaiian alkali basalt (C. P. Conrad, personal communication, 2014; Morgan & Liang, 2003). Details concerning the preparation of samples and deformation assembly are summarized in Qi et al. (2015). After fabrication, the undeformed samples have an average melt fraction of 0.07.

A series of high-strain torsion experiments were performed to induce CPOs in the olivine aggregates. Samples were deformed at $T = 1{,}473$ K and $P = 300$ MPa in a gas-medium apparatus fitted with a torsion actuator (Paterson & Olgaard, 2000) to outer-radius, R, shear strains of $2.6 \leq \gamma(R) \leq 13.3$. The torsion experiments were performed at a constant twist rate, yielding outer-radius shear strain rates, $\dot{\gamma}(R)$, of $\sim 10^{-4}$ s^{-1} for olivine + MORB samples and $\sim 10^{-3.5}$ s^{-1} for olivine + alkali basalt samples. After achieving the target strain, each sample was cooled rapidly (~2 K/s) to 1,300 K under the same torque as imposed at the end of the deformation experiment to preserve the deformation-produced microstructure and then cooled to room temperature with no torque applied. After deformation, samples have an average melt fraction between 0.04 and 0.06 (e.g., Qi et al., 2013, Table 1, experiment 0609).

Table 1
Summary of Experiments

Sample	Melt	$\sigma_{eq}(R)$ (MPa)	$\dot{\varepsilon}_{eq}(R)$ (s^{-1})	$\gamma(R)$	d^a (μm)	EBSD section
PT0609	MORB	160	7.8×10^{-5}	10	3.7	Tangential $\gamma \approx 9.1$, $\sigma_{eq} \approx 153$ MPa
PT0705	MORB	190	1.8×10^{-4}	13.3	3.1	Tangential $\gamma \approx 11.3$, $\sigma_{eq} \approx 176$ MPa
PT0765	Alkali basalt	177	2.2×10^{-4}	2.6	3.4	Tangential $\gamma \approx 2.4$, $\sigma_{eq} \approx 171$ MPa
PT0767	Alkali basalt	187	2.3×10^{-4}	11.1	3.1	Tangential $\gamma \approx 10.1$, $\sigma_{eq} \approx 180$ MPa Radial $0 \leq \gamma \leq 11.1$ Transverse $\gamma \approx 0$
PT0775	Alkali basalt	176	1.5×10^{-4}	8.5	3.5	Tangential $\gamma \approx 7.8$, $\sigma_{eq} \approx 170$ MPa
PT0817	Alkali basalt	197	2.3×10^{-4}	5.0	3.6	Tangential $\gamma \approx 4.6$, $\sigma_{eq} \approx 190$ MPa

Note. EBSD section refers to the section and its corresponding shear strain and equivalent stress that EBSD data is collected. [a]*d* is the grain size measured from the tangential section of each sample.

2.2. Mechanical Data and Rheology

Rotation angle and torque were recorded as a function of time during each experiment to determine shear stress, τ, shear strain, γ, and shear strain rate, $\dot{\gamma}$. To determine τ, corrections to the measured torque were made to account for the strength of the Fe jacket and Ni canister. τ was then calculated from the corrected torque, *M*, using the relationship (Paterson & Olgaard, 2000)

$$\tau = \frac{\left(3+\frac{1}{n}\right)M}{2\pi R^3}, \tag{1}$$

where the value of the stress exponent, *n*, is characteristic of the deformation mechanism. The rotation angle was converted to γ by taking into account the sample dimensions. Equivalent stress, σ_{eq}, and equivalent strain rate, $\dot{\varepsilon}_{eq}$, were calculated from τ and $\dot{\gamma}$ using the relationships

$$\sigma_{eq} = \sqrt{3}\tau \text{ and } \dot{\varepsilon}_{eq} = \frac{\dot{\gamma}}{\sqrt{3}}. \tag{2}$$

The results were then fit to a power law constitutive equation of the form

$$\dot{\varepsilon}_{eq} \propto \sigma_{eq}^n. \tag{3}$$

Strain-rate stepping tests were performed to determine *n*. In each strain-rate-step experiment, after the sample was sheared at a constant strain rate, $\dot{\gamma}_0$, to a strain large enough to produce a steady state microstructure and an approximately constant flow stress, the strain rate was increased or decreased to a new value, $\dot{\gamma}_1$, and held constant until the peak stress was reached. The strain rate was then returned to $\dot{\gamma}_0$ and maintained for a period of time to recover the steady state microstructure. For two samples, multiple strain rate steps were made.

Within a torsion sample, shear strain rate increases linearly with increasing radius, *r*. If the deformation mechanism does not change from $\dot{\gamma}(0) = 0$ at the center of the sample to its maximum value of $\dot{\gamma}(R) = \dot{\gamma}_{max}$ at the outer radius, then (Paterson & Olgaard, 2000)

$$\tau(r)/\tau(R) = \left(\frac{r}{R}\right)^{1/n}. \tag{4}$$

2.3. Analysis of Crystallographic Orientations

After each deformation experiment, polished sections of the sample were prepared for analyzing the crystallographic orientations. First, the iron jacket and the nickel capsule were dissolved with acid, revealing the strain marker that had been introduced as a shallow scratch on the outer surface of the sample prior to the deformation experiment. Then, for each sample, a tangential section was cut. In addition, for one sample, a transverse section and a radial section were cut through its axial center. The location of the tangential, transverse, and radial sections are illustrated in Figure 2a. Each section was polished down to a diamond grid size of 0.5 μm, followed by a final step with colloidal silica.

To obtain crystallographic orientation data, high-resolution orientation maps with a relatively small step size of 0.35 or 0.5 μm were collected for all sections using a scanning electron microscope equipped with

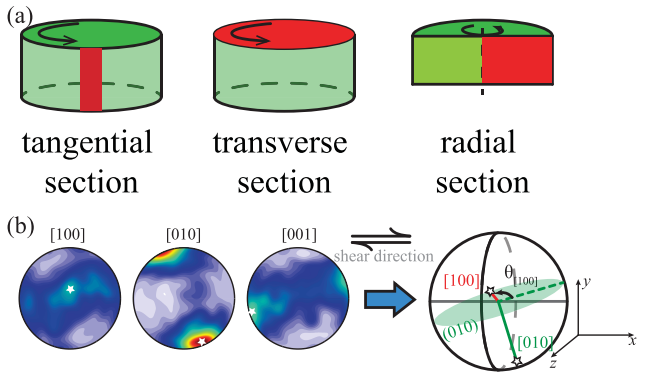

Figure 2. (a) Sketches illustrating tangential, transverse, and radial sections used in this paper. (b) Sketch illustrating the determination of the [100]-axes angle from a pole figure. White stars on pole figures show the modal orientations.

electron-backscattered diffraction (EBSD) system. Raw orientation data were processed with HKL Channel5 software, including removal of single misindexed points, assigning unindexed points the average orientation of neighboring grains, and removal of systematic misindexed points, as outlined in previous studies (e.g., Bystricky et al., 2006; Hansen et al., 2011). Orientation distributions were generated using the MTEX toolbox in MATLAB (Bachmann et al., 2010). Each orientation distribution was derived from at least 500 individual grains. A critical misorientation angle of 10° was used to separate grains. Clusters of less than five pixels were omitted from calculations of grain size values for each sample. The mean grain size for each sample was determined by taking the mean of the equivalent diameter of the grains calculated from the area.

To quantify the orientations of crystallographic axes relative to the shear direction, the angle θ is introduced as the angle between the shear direction in the (010) plane and the modal orientation of a certain group of crystallographic axes, as illustrated in Figure 2b. For example, to obtain $\theta_{[100]}$, a great circle (green ellipse in Figure 2b), that is, the (010) plane, was first fit normal to the modal orientation of [010] axes (solid green line). Next, the intersection between the (010) plane and *x*-*y* plane is taken as the shear direction in the (010) plane (dashed green line). Then the angle between the dashed green line and the modal orientation of [100] axes (red line) is $\theta_{[100]}$. By comparing the angles within the (010) plane, the distortion from the counterclockwise rotation of the fabric is minimized. For a typical A-type fabric, $0 \leq \theta_{[100]} \leq 20^\circ$ and $70^\circ \leq \theta_{[001]} \leq 90^\circ$.

To quantify the strength of the fabrics, both the J-index (Bunge, 1982) and the M-index (Skemer et al., 2005) were used. From uniformly distributed orientations to a single crystal orientation, the J-index, based on a calculated orientation distribution function, increases from 0 to infinity, while the M-index, based on the distribution of uncorrelated misorientation axes, increases from 0 to 1.

To quantify the shape of the distribution of crystallographic axes in pole figures, an eigenvalue analysis following Woodcock (1977) was employed. Normalized eigenvalues, S_1, S_2, and S_3, calculated from the orientation tensor, have relationships

$$S_1+S_2+S_3=1 \tag{5}$$

and

$$S_1 \geq S_2 \geq S_3. \tag{6}$$

The shape factor of the distribution of axes, K, is then defined by

$$K=\frac{\ln(S_1/S_2)}{\ln(S_2/S_3)}. \tag{7}$$

On a pole figure, $K > 1$ indicates that the distribution of axes forms a cluster, and $K < 1$ indicates that the distribution of axes forms a girdle.

2.4. Analysis of Geometrically Necessary Dislocations

To identify and quantify the dislocation types giving rise to lattice curvature, that is, the geometrically necessary dislocations, GNDs, in olivine within a sheared partially molten sample, we carried out high-angular resolution EBSD analysis (HR-EBSD) (Wilkinson et al., 2006). An EBSD map of 250 × 175 points at a step size of 0.2 μm was collected from within a melt-rich band on the transverse section of sample PT0767. Diffraction patterns were collected with 2 × 2 binning of CCD pixels and saved for HR-EBSD processing. The transverse section was chosen so that most [100] and [001] directions are at low angles to the plane of the map, which is overall the optimal configuration for measuring curvature arising from dislocations with these Burgers vectors (Wallis et al., 2016; Wheeler et al., 2009). HR-EBSD utilizes image cross correlation of diffraction patterns to achieve precisions on the order of 0.01° in measurements of lattice orientation gradients (Wilkinson et al., 2006). This improved angular resolution lowers the noise floor of associated GND density

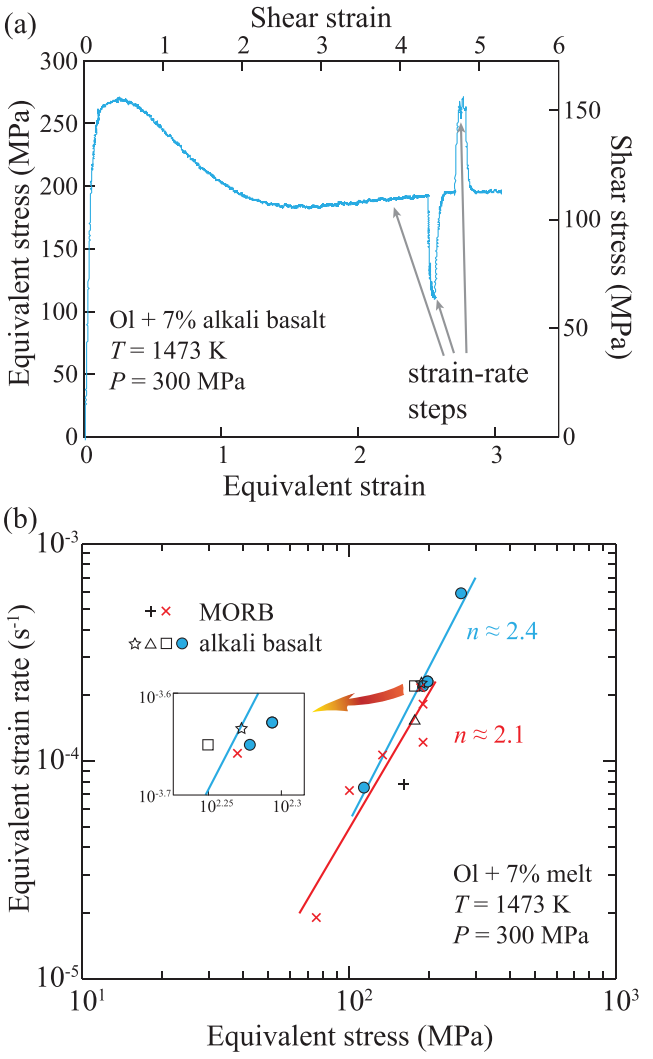

Figure 3. Mechanical data for samples of olivine + melt deformed in torsion at T = 1,473 K and P = 300 MPa. (a) Plot of stress versus strain for a sample of olivine + alkali basalt. Three different strain-rate steps were obtained during deformation. (b) Log-log plot of equivalent strain rate vs. equivalent stress for all samples used in this study. The solid lines are linear least square fits to multiple strain-rate steps obtained for two samples. Colors of lines corresponds with colors of data points (blue—PT0817, red—PT0705). The stress exponent, n, is indicated for each fit in the figure. Samples: PT0609: +, PT0705: × (in red), PT0765: △, PT0767: ☆, PT0775: □, and PT0817: ○ (filled in blue).

estimates, permitting more details of the substructure to be resolved than would be possible using misorientation measurements from conventional EBSD (Jiang et al., 2013; Wallis et al., 2016). Lattice orientation gradients were converted to lower-bound estimates of GND densities following the approach of Wallis et al. (2016, 2017), who considered six dislocation types.

2.5. Analysis of Grain Shape

EBSD data were analyzed with HKL Channel5 software to reconstruct the grain structure, defining grain boundaries as interfaces with misorientations of >10°. Each grain was fit with an ellipse to obtain its aspect ratio and orientation. Then, in each of the tangential, radial and transverse sections, grains were organized into two groups with respect to their crystallographic orientations—[100] axes subparallel and [100] axes subnormal to shear direction. The selection was performed in HKL Channel5 software by picking a subset of grains with crystallographic orientations that lay within ~20° around the target crystallographic orientation. Grains with an area of less than 2 μm^2 were excluded, since they do not contain enough pixels to derive reliable values of aspect ratio and slope of the ellipse. Each group contained 600–2,200 grains. For each group of grains, the SPO is illustrated by a rose diagram, and the distribution of aspect ratios is illustrated by a histogram. Thus, the shapes are obtained for grains with selected crystallographic orientations for comparison with the associated CPOs.

3. Results

3.1. Mechanical Data

To facilitate comparison of CPOs from different samples, all samples were deformed at an equivalent outer-radius strain rate of $\dot{\varepsilon}_{eq}(R) = (2.0 \pm 0.5) \times 10^{-4}$ s^{-1} producing an equivalent outer-radius stress of $\sigma_{eq}(R) = 187 \pm 11$ MPa, with the exception of sample PT0817. The stress exponents determined from strain-rate-step experiments are $n \approx 2.1$ for PT0705 and $n \approx 2.4$ for PT0817, as illustrated in Figure 3. Mechanical data and EBSD mapped sections for all samples are summarized in Table 1.

The shear strain of each sample was determined by multiplying applied strain rate with time and by measuring the angle of the strain marker relative to shear direction; the two methods gave the same result. No axial shortening or lengthening was found in these samples.

3.2. CPO Evolution with Radius

To investigate the evolution of CPO with increasing radius in a partially molten rock deformed in torsion, nine individual orientation maps from a radial section of sample PT0767 were stitched together. This orientation map, which is presented in Figure 4a, covers a 6 mm long by 0.2 mm wide section extending from the center to the edge of the sample, with shear strain increasing from 0 to 11.1. With a step size of 0.5 μm, this map contains 177 thousand grains and 2.4 million data points with <15% unindexed. With the shear stress at the outer radius $\tau(R) \approx 108$ MPa as calculated by equation (1), τ at radius r calculated using equation (4) with $n \approx 2.4$ is plotted in Figure 4b. Due to base-state melt segregation that occurs in partially molten rocks deformed in torsion (Takei & Katz, 2013), the melt fraction gradually decreases with increasing radius, as demonstrated for sample PT0767 in Figure 4b (for details, see Qi et al., 2015).

In the low-resolution orientation map in Figure 4a and the much larger full-resolution map in the online supporting information, grains are colored by orientations of [100] axes, with green representing [100] axes

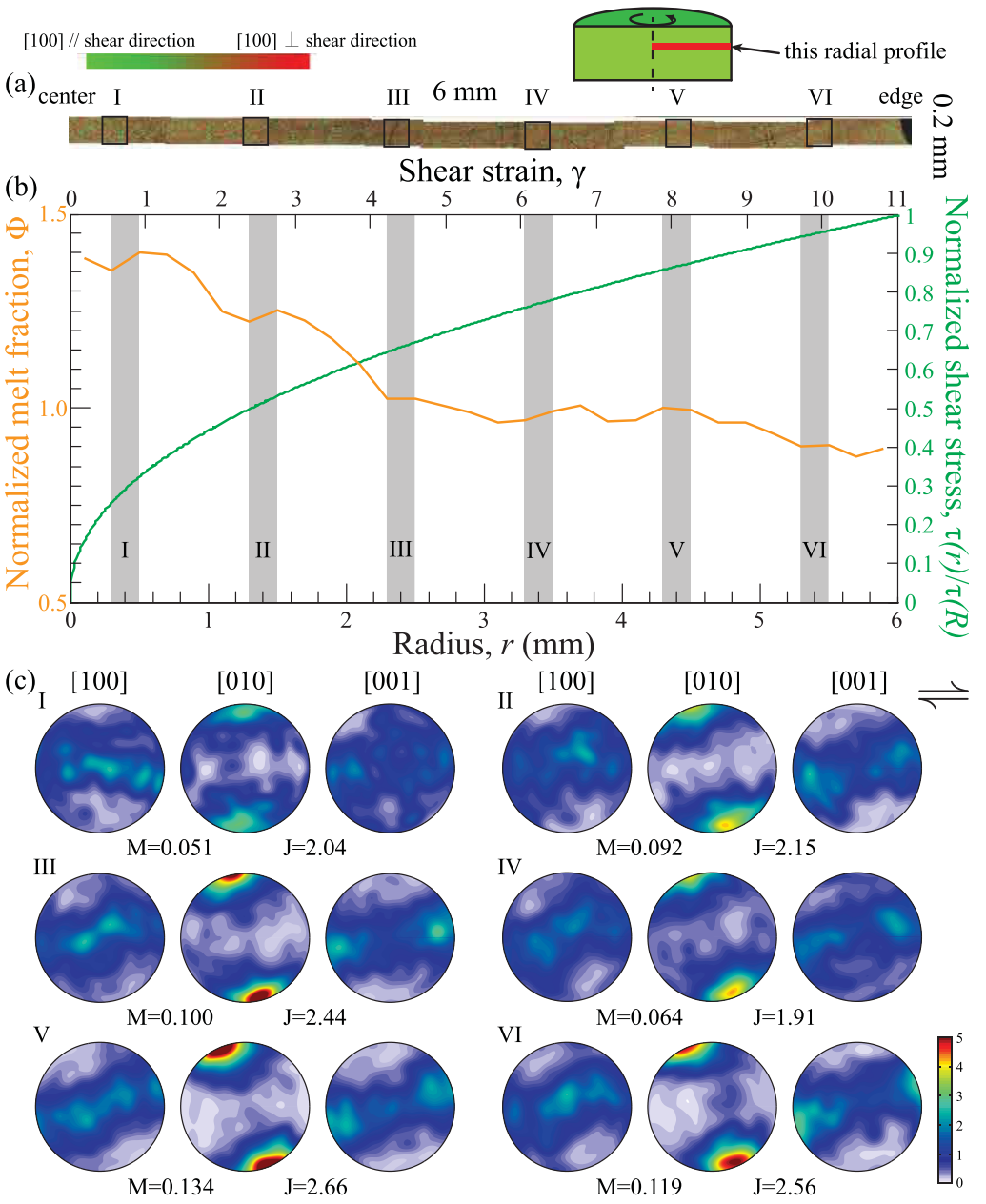

Figure 4. (a) Orientation map for a radial section of sample PT0767. (b) Plot of shear stress and melt fraction vs. radius. Shear stress is normalized to the shear stress at the outer edge, $\tau(R) \approx 108$ MPa. Melt fraction is normalized to its average, 0.05. (c) Six sets of pole figures at different radii, with their corresponding regions marked in both the orientation map in Figure 4a and the plot in Figure 4b. Each pole figure is processed from more than 1000 grains using MTEX toolbox in MATLAB (Bachmann et al., 2010). Pole figures are universally colored by their multiples of uniform distributions (MUD), which is illustrated in the color bar. The maximum and minimum values of MUDs are listed for each pole figure. The sense of shear for the pole figures is top to the right. J- and M-indexes are included for each region.

aligned parallel to the shear direction and red representing [100] axes aligned normal to the shear direction. Pole figures processed from orientation data of six evenly spaced regions from the radial section, which are marked by rectangles on the map in Figure 4a and gray bars on the plot in Figure 4b, provide a clear illustration of fabric evolution along the radius. For easy comparison with results obtained from analyses of other sections, the deformation geometry in these pole figures is converted such that the sense of shear is top to the right in Figure 4c. Except for pole-figure set I for $\gamma < 1$, which has clustered [010] axes aligning normal to the shear plane, all other sets of pole figures feature strongly clustered [010] axes rotated 20–25°

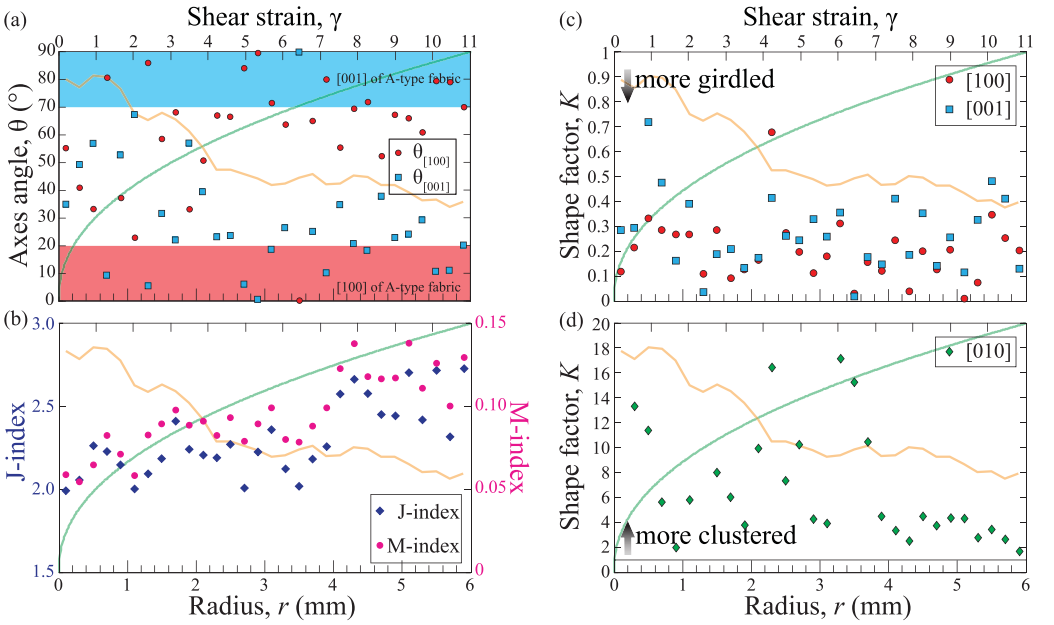

Figure 5. Evolution of fabric with radius for a radial section of a sample sheared to $\gamma(R) = 11.1$ (PT0767). The translucent orange and green curves in the background of plots (a)–(d) are the changes with radius of melt fraction and stress, respectively, from Figure 4. (a) Plot of axes angles vs. radius. The red and blue shades in the plot suggest $\theta_{[100]}$ and $\theta_{[001]}$ for a typical A-type olivine fabric. (b) Plot of J- and M-indexes vs. radius. (c) Plot of shape factor *K* for the distributions of [100] and [001] axes versus radius. (d) Plot of shape factor *K* for the distribution of [010] axes versus radius. The gray horizontal line is $K = 1$.

counterclockwise from the normal to the shear plane combined with weakly girdled [100] and [001] axes. Although [100] and [001] axes are girdled, the modal orientation of [001] axes is consistently at a low angle to the shear direction, while the modal orientation of [100] axes is subperpendicular to the shear direction in the shear plane. For pole-figure sets II–VI, although $\tau(r)$ increases from ~54 to ~102 MPa and $\gamma(r)$ increases from ~2.5 to ~10, the strength and shape of the fabric change very little.

The variation in the orientations of [100] and [001] axes with radius documents the occurrence of the a-c switch, as presented in Figure 5a. For each data point in this figure, $\theta_{[100]}$ and $\theta_{[001]}$ were calculated using orientation data of a 200 × 200 μm region in the radial section. At $r > 2.2$ mm ($\gamma > 4$), values of $\theta_{[100]}$ are mostly above 60°, far from the value of 0° to 10° expected for the A-type fabric produced by the (010)[100] slip system. In the same region, values of $\theta_{[001]}$ are mostly between 10° and 40°, again, far from the range of 70° and 90° for the A-type fabric. Thus, the high angle of $\theta_{[100]}$ and the low angle of $\theta_{[001]}$ indicate that at $r > 2.2$ mm a CPO is established with a somewhat stronger alignment of [001] than [100] axes in the shear direction.

As illustrated in Figure 5b, the J-indexes and M-indexes both increase with increasing radius. However, across this radial section, which spans a shear strain of 0–11, the increases in both texture indexes are modest, ~0.8 for the J-index and ~0.09 for the M-index, relative to the strength of A-type fabrics, which have been recorded to have J-indexes and M-indexes with values up to 29.4 and 0.69 at a shear strain of 11 (Hansen et al., 2014).

In Figures 5c and 5d, the shape factors for the distributions of crystallographic axes are plotted versus radius. The distributions of [100] and [001] axes remain in the girdled field ($K < 1$) for all radii with slight variation along radius. The distribution of [010] axes remains in the clustered field ($K > 1$) for all radii. The value of *K* for [010] axes varies significantly for $r < 4$ mm but becomes steady for $r > 4$ mm.

3.3. CPO Evolution With Strain

Observations from tangential sections of six samples deformed to shear strains of $2.4 \leq \gamma \leq 11.3$ offer insight into the evolution of CPO with strain. In particular, results from the four olivine + alkali basalt

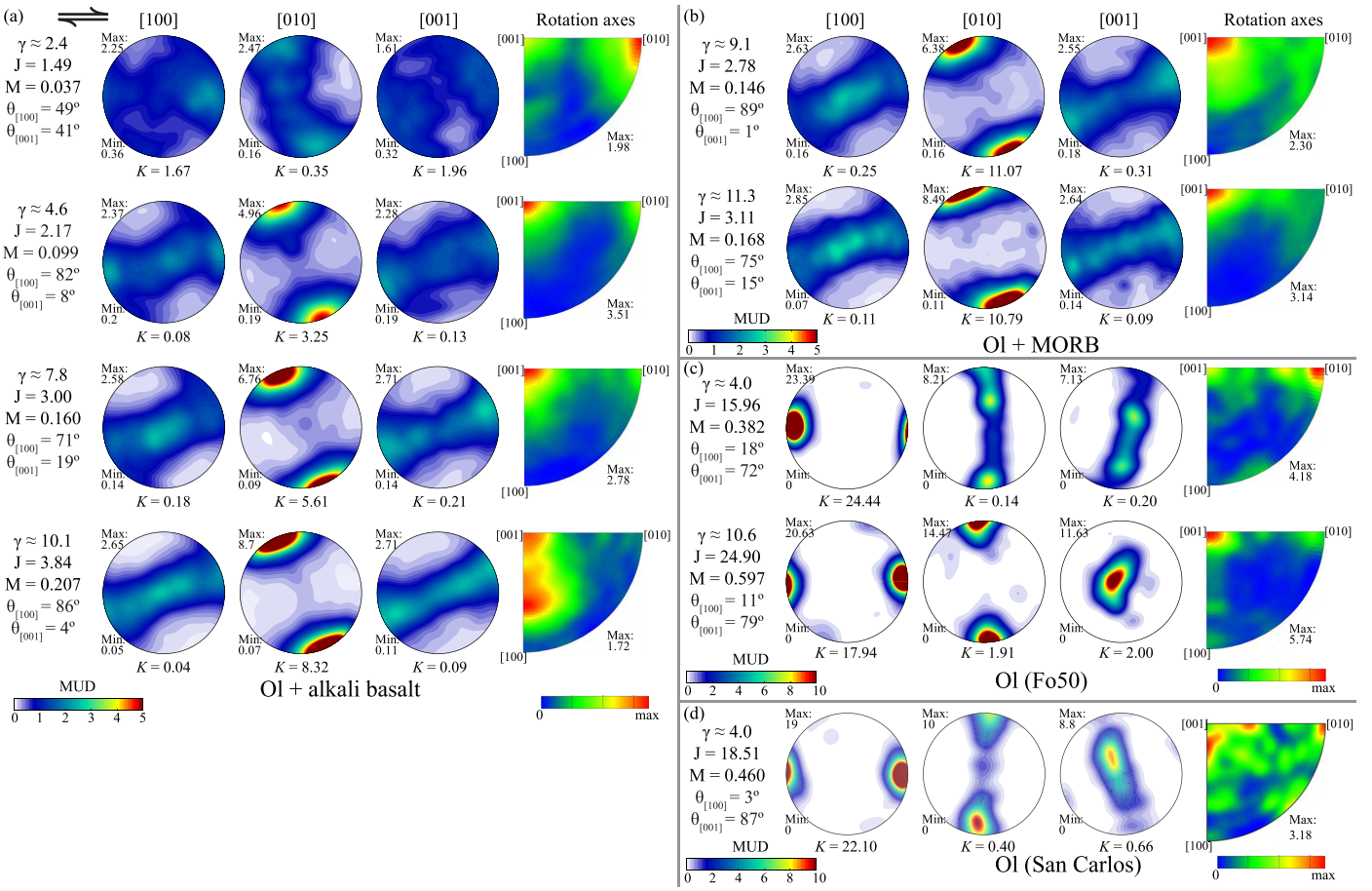

Figure 6. Pole figures of crystallographic orientations and plots of rotation axes at subgrain boundaries (2–10°) for tangential sections at different strains. J-index, M-index, $\theta_{[100]}$ and $\theta_{[001]}$ are calculated based on the complete orientation data for each section. *K* is calculated for each crystallographic axis. (a) Results from samples of olivine + alkali basalt. (b) Results from samples of olivine + MORB. (c) Results from deformed samples of Fo50 for comparison (Hansen et al., 2014, samples PT0640 and PT0651). (d) Results from deformed samples of San Carlos olivine for comparison (Tielke et al., 2016, samples PT0951).

samples, which were deformed at approximately the same shear strain rate, and thus, similar stresses, provide a suitable basis for the investigation of the evolution of CPOs with strain.

In the top pole figure in Figure 6a from a sample with the tangential section at $\gamma \approx 2.4$, although the crystallographic fabric is weak with J-index = 1.49 and M-index = 0.037, the distribution of [010] axes displays a counterclockwise rotation from the normal to the shear plane. However, at this strain, no clear preference exists for alignment of [100] or [001] with the shear direction. In contrast, in the pole figures in Figures 6a and 6b from the five samples deformed to $\gamma > 4$, the [100] and [001] axes form a girdle with a weak but clear alignment of [001] axes at a low angle to the shear direction. Again, the [010] axes form a cluster rotated counterclockwise from the normal to the shear plane.

As summarized in Figures 6a and 6b for the five samples deformed to $\gamma > 4$, the angle $\theta_{[100]}$ varies between 71° and 89°, and $\theta_{[001]}$ varies between 1° and 19°; neither angle shows an obvious correlation with increasing strain. The J-indexes and M-indexes generally increase with increasing strain, and the olivine + alkali basalt samples have somewhat stronger fabrics than olivine + MORB samples at similar strains.

To further explore fabric evolution with increasing strain, orientation data from all six samples are plotted in $\ln(S_1/S_2)-\ln(S_2/S_3)$ space (see equation (7) in section 2.3) for the three principal crystallographic axes in Figure 7. In this plot, fabric strength, which increases with increasing distance from the origin, clearly increases with increasing strain for all three principal crystallographic axes. At all strains, [100] and [001] axes have similar fabric strengths, but both are smaller than those of the [010] axes. The distribution of [010] axes starts as a girdle at $\gamma \approx 2.4$, then evolves to a cluster at $\gamma > 4$; that is, for [010] axes, the shape factor *K*, which is the slope of

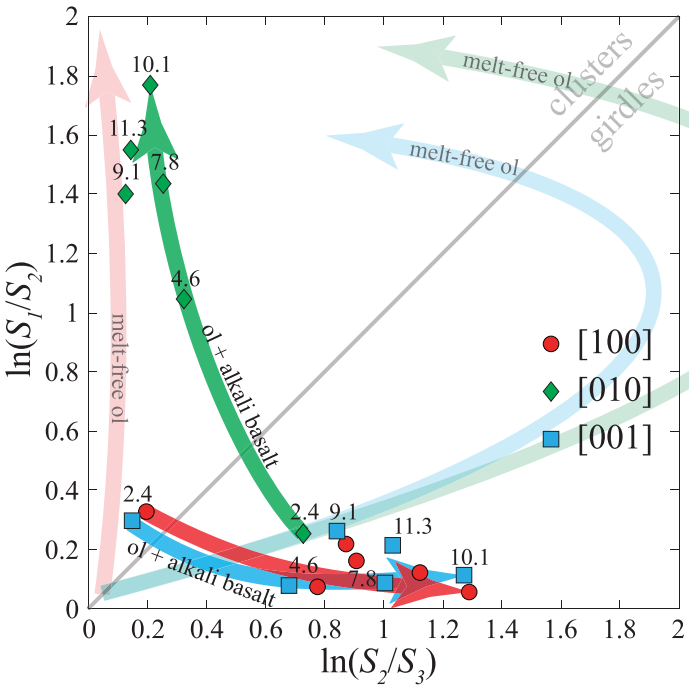

Figure 7. Evolution of crystallographic fabric strength and shape with strain. S_1, S_2, and S_3 are the eigenvalues of the orientation tensor as defined by Woodcock (1977). Fabric strength increases with increasing distance from the origin. The degree of clustering/girdling increases with proximity to the ordinate/abscissa. Shear strain is marked for each data point in the plot. The bold-colored arrows indicate the trend of fabric evolution with strain in olivine + alkali basalt samples, with their colors corresponding to the crystalline axes. The light arrows are the trends of fabric evolution with strain in dry, melt-free olivine samples from Hansen et al. (2014).

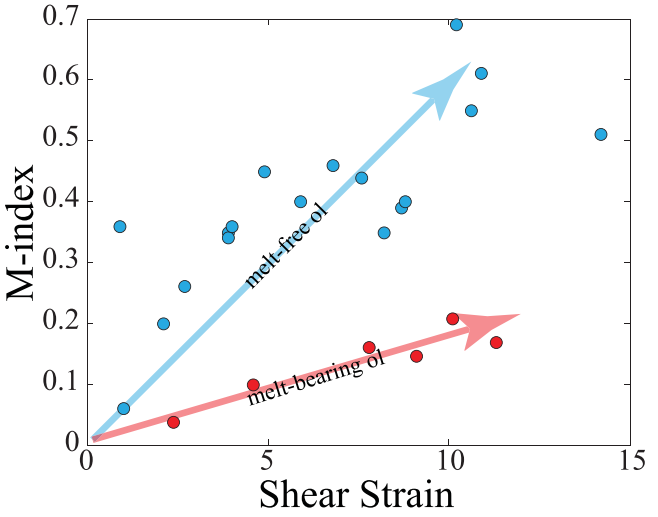

Figure 8. Evolution of M-index with strain. Red dots represent the melt-bearing olivine samples in this study. Blue dots represent dry, melt-free olivine samples from Hansen et al. (2014). Arrows mark the trends of M-index evolution with shear strain.

the line that connects the data point to the origin, increases with increasing strain. The distributions of [100] and [001] axes share a similar trend, starting as clusters at $\gamma \approx 2.4$ and becoming girdled at $\gamma > 4$. However, K for [100] and [001] axes does not change with increasing strain for $\gamma > 4$. In Figure 7, the evolution paths for the principal axes of the four samples of olivine + alkali basalt series are indicated by bold-colored arrows, while the light arrows correspond to trends in melt-free samples (Hansen et al., 2014).

To further reveal the differences in the evolution of fabric strength with increasing strain for melt-bearing and melt-free olivine, M-indexes of samples in this study and in Hansen et al. (2014) are plotted with shear strain in Figure 8. At similar strains, M-indexes of melt-bearing olivine are lower than those of melt-free olivine. M-index increases with increasing strain in both groups of samples; however, the rate of increase of the M-index with increasing strain is larger for melt-free olivine than for melt-bearing olivine.

3.4. CPOs In and Out of a Melt-Enriched Band

To examine the influence of melt-enriched bands on CPO, pole figures were processed from a melt-enriched band region and a melt-depleted nonband region in a tangential section at $\gamma \approx 9.1$ of an olivine + MORB sample (PT0609). The comparison in Figure 9 of the pole figures from these two regions reveals the following: (i) The general orientations and distributions of crystallographic axes are similar in the two regions. (ii) In terms of the J-indexes and M-indexes, the strength of the crystallographic fabric in the nonband region is somewhat stronger than that in the band region. (iii) The counterclockwise rotation of the modal distribution of [010] axes in the band region is more than 10° smaller than in the nonband region (16° versus 30°). (iv) In the band and nonband regions, the average grain sizes are 3.1 and 3.6 μm, respectively.

3.5. Densities of GNDs

The maps of GND densities for six principle dislocation types in olivine in Figure 10 reveal complex intragranular substructures composed of subgrain boundaries and distributed dislocations. Many structures are composed of several dislocation types, indicating a prevalence of both subgrain boundaries and distributed lattice curvature with mixed character. Edge dislocations of the type (010)[100] are the most ubiquitous and contribute to nearly all of the visible substructures. The mean density of (010)[100] edge dislocations, 2.8×10^{13} m^{-2}, is 1.5 to 2.2 times greater than the density of any of the other dislocation types. The map of GND densities for our deformed partially molten samples in Figure 10 is similar to the map of GND densities of melt-free olivine samples, as illustrated in Figure S2 in the supporting information.

3.6. Grain Shape and Crystallographic Orientation

To explore the possibility that grain shape is crystallographically controlled, as is the case for olivine grains in a basaltic melt, grain shape and crystallographic orientation were examined for three orthogonal surfaces of an olivine + alkali basalt sample (PT0767) deformed to $\gamma(R) = 11.1$. The orientations of the crystallographic axes of selected grains are examined in Figure 11 with pole figures, rose diagrams of the orientations of grain long axes, and histograms of aspect ratios. Consider, for example, Figure 11a, the light gray girdles and clusters in the background represent the overall CPO observed in this section. The yellow stars in the pole

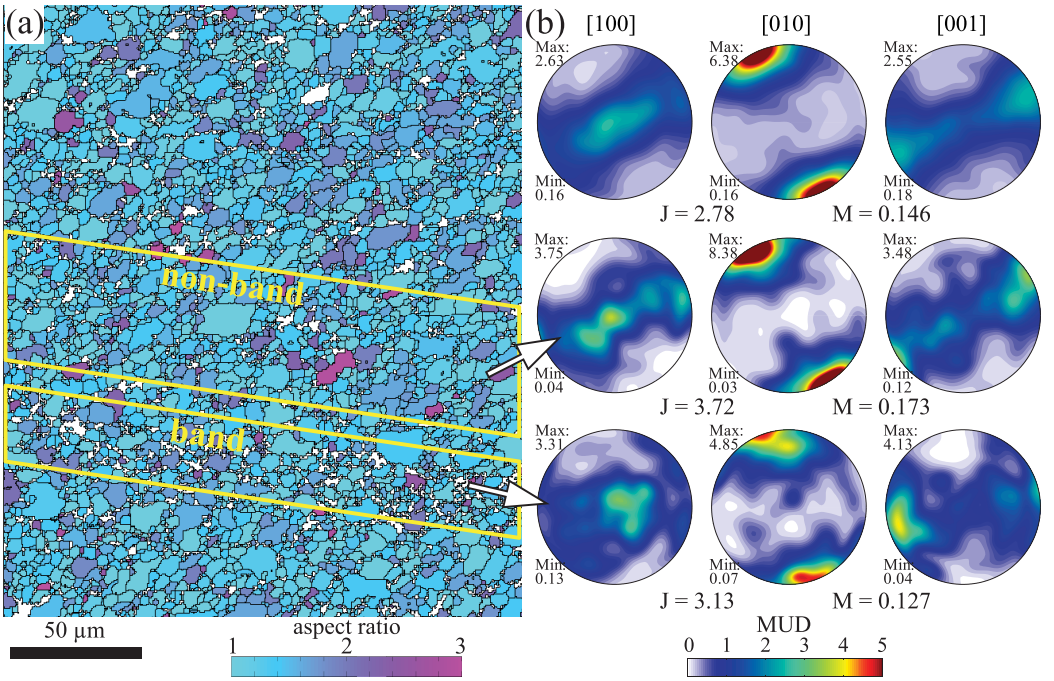

Figure 9. Comparison of CPOs in a melt-enriched "band" region and in a melt-depleted "nonband" region in the tangential section of sample PT0609. (a) The orientation map is colored by the aspect ratios of grains. White pixels are unindexed points, which are taken as melt. The parallelogram-shaped region noted as "band" is a melt-enriched band. The parallelogram-shaped region noted "nonband" is a melt-depleted region. (b) From top to bottom, the three sets of pole figures are for the whole section, nonband region and band region, respectively.

figures indicate the reference orientation for the subset of grains used to make the other plots in this panel. The subset of grains was selected with [010] and [001] axes distributed in the regions indicated by blue points, such that the orientations of these grains lie within 20–30° to the target orientation. Each grain in this subset is fitted with an ellipse with its long-axis orientation plotted in the rose diagram and aspect ratio plotted in the histogram. This information permits a comparison of the preferred orientations of crystallographic axes with the orientation of long axes of grains.

In tangential sections, since [010] axes form strong point maxima subperpendicular to the shear plane, comparisons are only obtained between the relative lengths of grains along [100] and [010] axes, Figure 11a, and between the relative lengths of grains along [001] and [010] axes, Figure 11b; these comparisons reveal that grains are shortest along [010] axes. In radial sections, Figures 11c and 11d, again grains are observed to be shortest along [010] axes. In transverse sections, the relative lengths of grains along [100] and [001] axes are compared. In Figure 11e, the modal orientation of the long axes correlates the modal orientation of [001] axes, indicating that grains are longer along [001] axes than along [100] axes. In Figure 11f, it is notable that the modal orientation of the long axes is rotated 30° from the modal orientation of [001] axes. Note that this transverse section is at the center of sample PT0767, where very little deformation has occurred; thus, the grain shapes are unlikely to have been altered by deformation. The histograms for all sections demonstrate that the elongations of the grains are significant with an average aspect ratio of ∼1.5.

3.7. CPO and SPO

To examine the relationship between CPO and SPO for the five higher-strain ($\gamma > 4$) samples that exhibited the a-c switch, pole figures highlighting the CPOs and rose diagrams quantifying the SPOs are presented in Figure 12. Specifically, the modal orientations of [001] axes are compared to the SPOs because, as demonstrated in the previous section, grains are elongated along their [001] axis. For the sample deformed to the lowest strain in this group, $\gamma \approx 4.6$, the pole figures in Figure 12a exhibit a weak A-type fabric with [100] axes forming a weak point maximum subparallel to the shear direction. Meanwhile, the SPO lies ∼54° to the shear direction, strikingly different than the orientation of [001] axes. In contrast, for

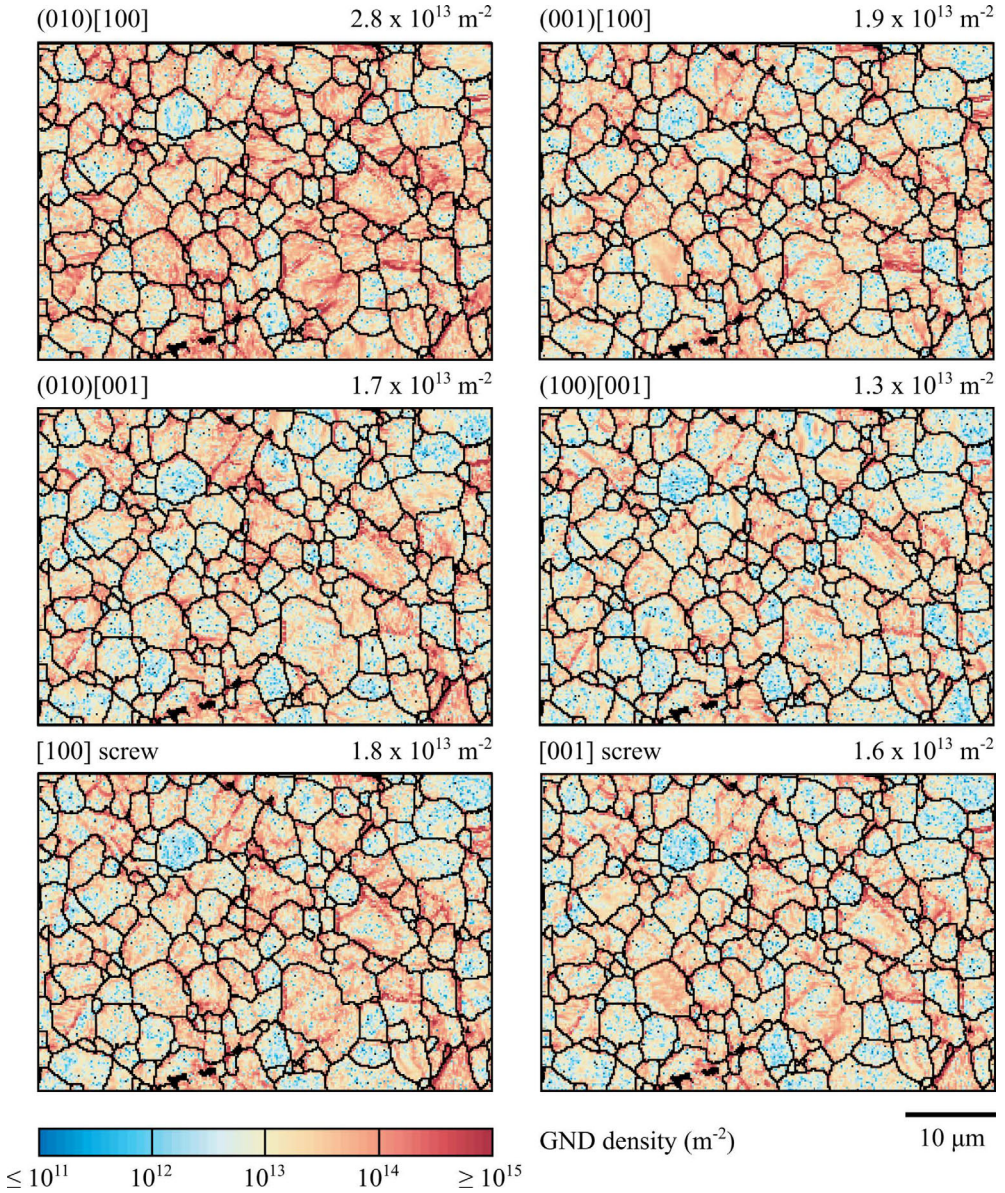

Figure 10. Maps of the density of geometrically necessary dislocations (GND) for the six principle dislocation types in olivine within a melt-rich band on a transverse section of PT0767. Also given is the mean density of each dislocation type across the map area.

samples deformed to $\gamma \geq 7.8$, the modal orientations of [001] axes and the SPOs both lie 21–30° to the shear direction.

4 Discussion

4.1. A Model to Explain the a-c Switch

In the previous section, our observations on samples deformed to high shear strains combined with previously published observations (Holtzman et al., 2003a; Kohlstedt & Holtzman, 2009) revealed two clear differences between the CPOs of olivine deformed in the absence and presence of 7 vol % basaltic melt. First, the CPOs of the olivine plus melt samples are always much weaker than those of single-phase olivine. Second, the a-c switch is evident by $\gamma \approx 4$ in the melt-bearing samples. The a-c switch is characterized by three key features—(i) girdles of [100] and [001] axes at a low angle to the shear plane, (ii) weakly aligned, shear-normal [100] axes in the shear plane, and (iii) antithetic rotation of the fabric with strongly aligned [010]

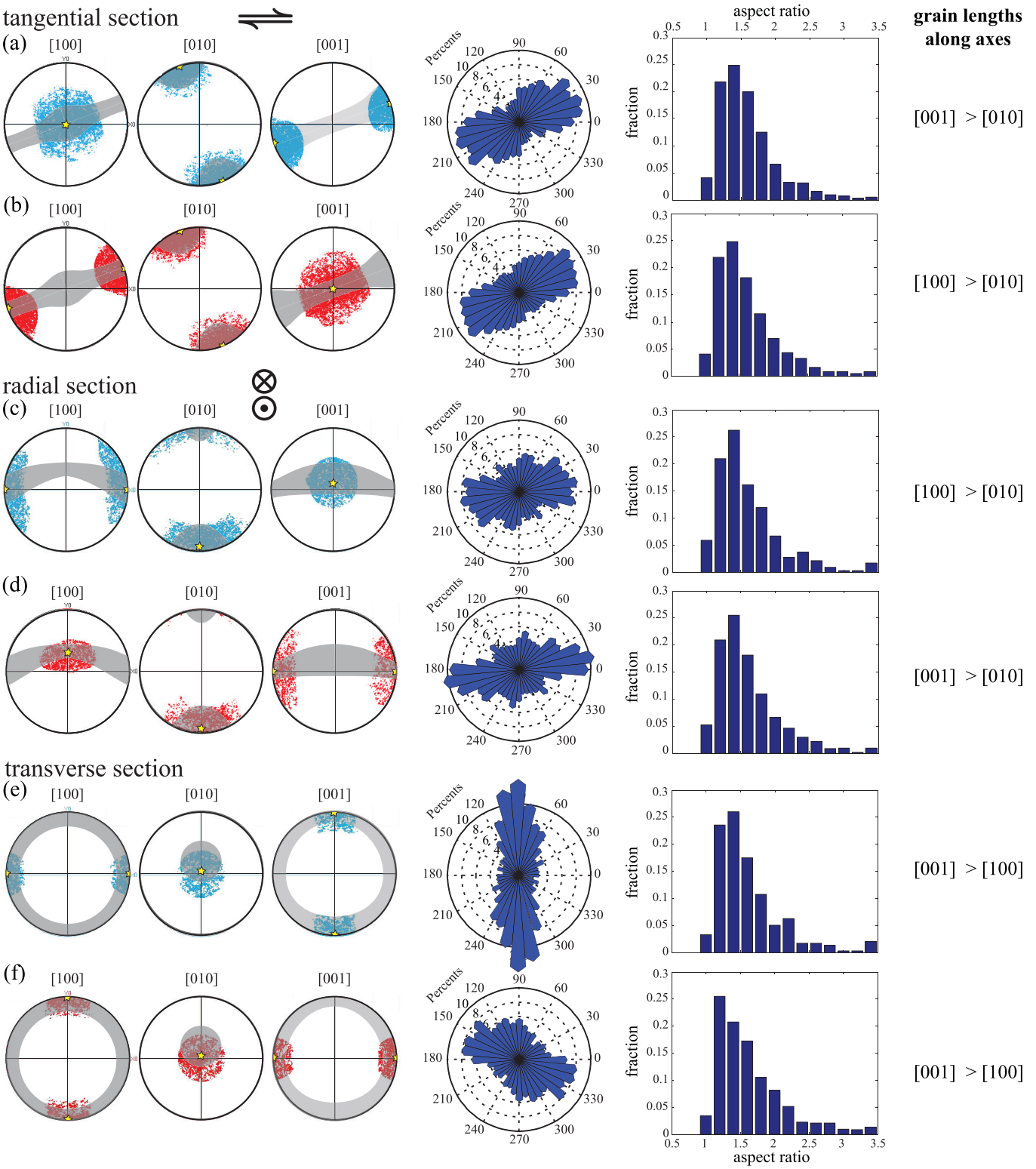

Figure 11. Comparison of orientation of crystallographic axes with direction of the long axes of selected subsets of grains. In plots (a)–(f), the blue and red points in the pole figures indicate the subsets of grains that were selected based on their crystallographic orientations, the rose diagrams show the orientations of the long axes of this subset of grains, and the histograms illustrate their aspect ratios. The gray regions in the pole figures represent the overall CPO, and the yellow stars represent the reference orientation of the subset of grains. In the rose diagrams, the length of each bar corresponds to the fraction of grains with a specific orientation. The relative lengths of grains along the three crystallographic axes are summarized in the far right-hand column.

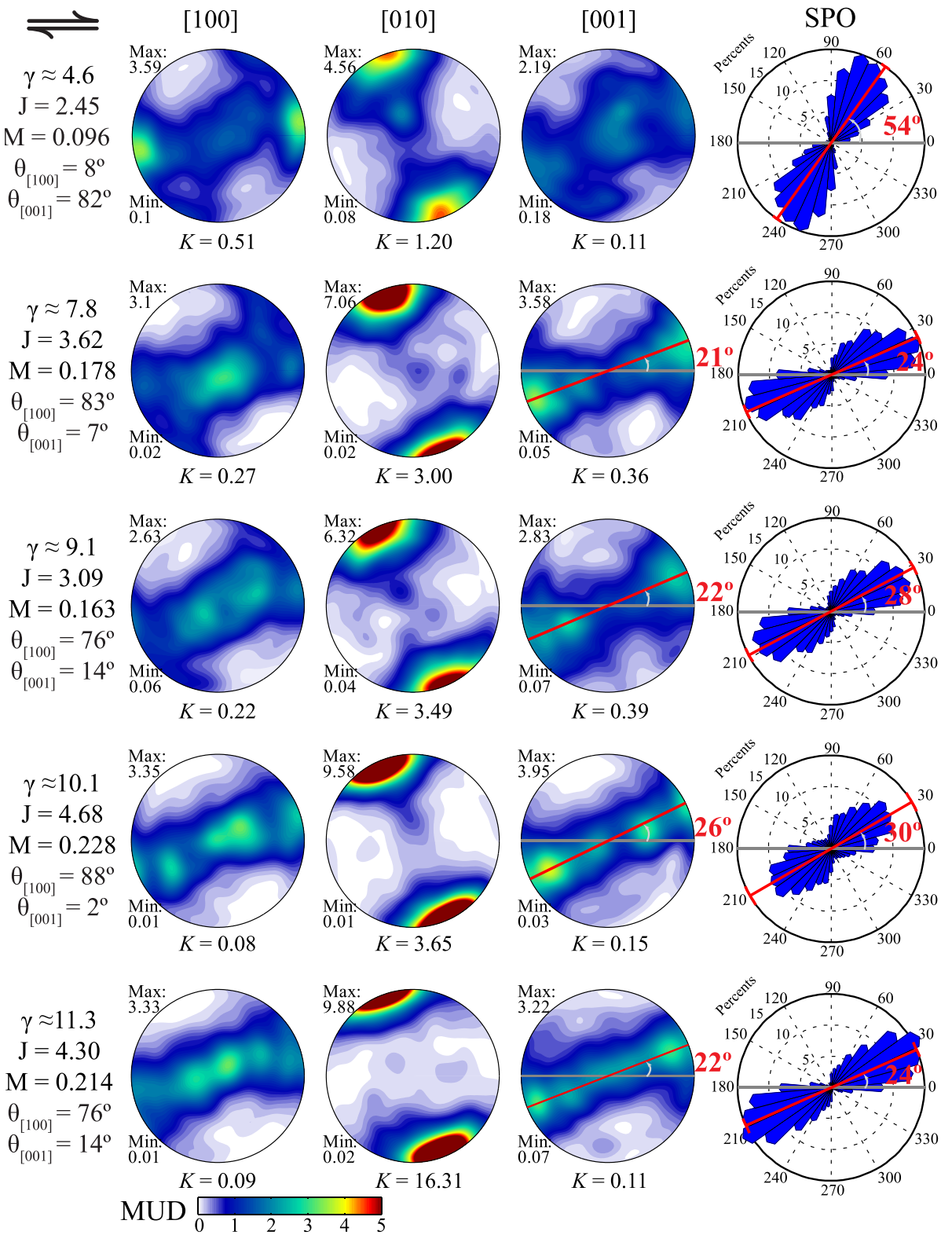

Figure 12. The relationship between SPO and CPO observed in tangential sections of the five samples sheared to $\gamma > 4$. Pole figures and rose diagrams are processed from grains with grain areas greater than 10 μm^2 and aspect ratios greater than 1.5. J-index, M-index, [100] axes angle, and [001] axes angle were calculated for each crystallographic fabric. Fabric shape factor K is calculated for each crystallographic axis. The angle, ψ, noted on each [001] pole figures lies between the shear direction and the projections of the modal orientations of [001] axes on the tangential surface (the plane of observation). The angle between the long axes of grains and the shear direction is noted on each rose diagram.

axes normal to the shear plane. In developing a model that explains these key features, we compare the CPOs observed in this study with those reported for melt-free olivine (section 4.1.1), review the explanation previously published for the antithetic rotation of the fabric (section 4.1.2), and discuss the evidence for a SPO-induced CPO (section 4.1.3). With the insights from these subsections, we establish a melt-assisted, SPO-induced CPO model (section 4.1.4) to explain the a-c switch.

4.1.1. Comparison of CPOs of Sheared Melt-Bearing and Nominally Melt-Free Samples

A comparison with the CPO formed in sheared samples of melt-free olivine provides insight into the mechanisms responsible for the CPOs observed in sheared samples of olivine plus melt. Pole figures for three samples of nominally melt-free olivine are presented in Figure 6c for Fo_{50} and Figure 6d for San Carlos olivine (Fo_{90}). Both Fo_{50} samples were deformed in torsion at $\sigma_{eq} = 200 \pm 5$ MPa and 1,473 K (Hansen et al., 2014), conditions comparable to those used in our study. The San Carlos olivine sample was deformed in torsion at $\sigma_{eq} = 197$ MPa and 1,523 K (Tielke et al., 2016), a stress comparable to those used in our study. We choose to compare the CPOs observed in melt-bearing olivine to that in melt-free Fo_{50} olivine for the following reasons. (1) As demonstrated in Figures 6c and 6d, Fo_{50} and San Carlos olivine exhibit the same CPO in samples deformed to the same strain at similar stresses. Also, it has been demonstrated that Fo_{50} is a good analog for San Carlos olivine in terms of CPO evolution (Hansen et al., 2014). (2) A good database of CPOs for Fo_{50} samples deformed at the same experimental conditions already existed (Hansen et al., 2014). (3) To keep the stress comparable to that used to deform melt-bearing olivine samples, San Carlos olivine samples have to be deformed at higher temperature, while Fo_{50} samples can be deformed at the same temperature as used in our experiments.

At similar strains, in addition to the obvious differences in the orientations of the crystallographic axes, two differences are striking: (1) Fabric strength is much higher in olivine samples than in olivine + melt samples; and (2) in the nominally melt-free samples, the distribution of [100] axes is strongly clustered, while the distributions of [010] and [001] axes are girdled at lower strains and clustered at high strains. In contrast, only the distribution of [010] axes is clustered in olivine + basaltic melt samples.

The evolution of crystallographic fabric shape for samples of olivine plus basalt is distinctly different from that for samples of melt-free olivine, as demonstrated in Figure 7 with bold and light arrows, respectively. In olivine samples, the distribution of [100] axes starts clustered and becomes more clustered with increasing strain, while the distributions of [010] and [001] axes start as girdles but become clustered at high strains. In contrast, in the olivine + alkali basalt samples, the distribution of [010] axes starts clustered and becomes more clustered with increasing strain, while the distributions of [100] and [001] axes start as girdles and remain girdled at high strains.

As illustrated in Figures 6a and 6b for partially molten samples, misorientation axes with misorientation angles between 2° and 10° tend to be aligned with [001] and, to a lesser extent, with [010]. This observation indicates that (010)[100] is the dominant slip system, assuming that subgrain walls have dominantly tilt character (Hildyard et al., 2009; Lloyd et al., 1997; Prior et al., 2002). Similar misorientation axes developed in sheared aggregates of nominally melt-free olivine samples (Hansen et al., 2014), as illustrated in Figure 6c. If the a-c switch is a result of a change of the easy slip system from (010)[100] to (010)[001], one would expect the misorientation axes to be aligned with [100], which is clearly not the case for the samples examined here. Thus, a mechanism other than a change in the dominant slip system must be responsible for the observed CPOs.

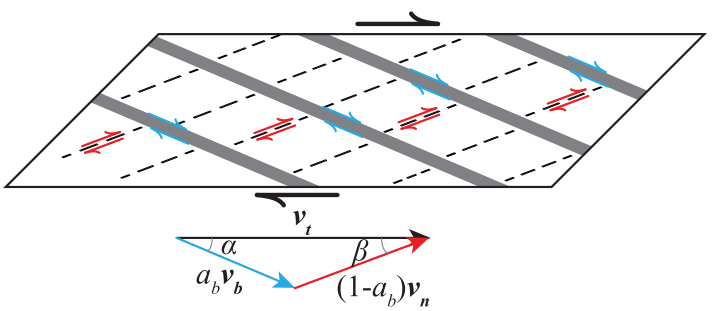

Figure 13. Schematic drawing illustrating strain partitioning. The thick gray lines represent the melt-enriched bands and the thin dashed lines represent the shear plane in the melt-depleted nonbands. The vector diagram below illustrates the relationship in equation (8). Modified after Holtzman et al. (2005).

4.1.2. Local Deformation Geometry

The counterclockwise rotation of [010] axes from the normal to the shear plane at $\gamma \gtrsim 2$ occurs due to strain partitioning between the melt-enriched and melt-depleted regions that result from stress-driven melt segregation (Holtzman et al., 2005). As illustrated schematically in Figure 13, an anastomosing network of melt-enriched bands in sheared partially molten rocks forms at an angle α to the imposed shear plane, synthetic to the bulk shear direction. These low-viscosity regions deform more easily than melt-depleted regions. However, because of strain incompatibility at the sample ends, the imposed horizontal shear direction requires the nonband regions to

accommodate shear strain at an angle β to the bulk shear plane, rotated antithetically to the imposed shear direction. The relationship between the flow velocities in the two different regions is

$$\vec{v}_t = a_b\vec{v}_b + (1-a_b)\vec{v}_n, \tag{8}$$

where $\vec{v}_t$ is the vector representing the flow velocity of the whole rock, $\vec{v}_b$ and $\vec{v}_n$ represent the flow velocities in the melt-enriched (band) and melt-depleted (nonband) regions, respectively, and a_b is the area fraction of the melt-enriched regions. A viscous energy dissipation analysis yielded $\beta \approx 20°$ (Holtzman et al., 2005; Katz & Takei, 2013; Takei & Holtzman, 2009; Takei & Katz, 2013), consistent with the observed counterclockwise rotation of [010] axes. Thus, the [010] axes are normal to the *local* shear plane, and [100] and [001] axes lie in the *local* shear plane in the melt-depleted portions of a sample, as the bands only take a small fraction of the total volume.

4.1.3. SPO-Induced CPO

A crystallographically controlled SPO can also induce a CPO (Miyazaki et al., 2013). Simple shear of elongate grains rotates the long axis of these grains toward the shear direction (Ghosh & Ramberg, 1976; Ildefonse et al., 1992a, 1992b), producing a SPO. If the elongate grain shape is crystallographically controlled, the SPO results in a CPO.

Since olivine grains in our samples are on average longest along [001] axes, a SPO-induced CPO would align [001] axes in the shear direction. In samples deformed to $\gamma \gtrsim 7$, the modal orientation of [001] axes approximately aligns with the SPO. Both lie between 20° and 30° to the applied shear direction in these samples, that is, approximately parallel to the local shear direction. Thus, the observed alignment of [001] in the local shear direction suggests that the SPO contributes to the CPO observed in our sheared partially molten rocks. Due to grain rotation, the shortest direction of the oblate ellipsoidal grains, [010], aligns approximately normal to the local shear plane.

4.1.4. Melt-Assisted SPO-Induced CPO Model

We propose that a SPO-induced CPO develops in our experiments. If such mechanism is the only one occurring, a CPO with [001] axes clustering parallel to the shear direction should develop. However, the observed CPO is manifested as a weak fabric in the shear plane with girdles in the orientations of the [100] and [001] axes suggesting a contribution to the CPO from dislocation glide on the (010)[100] slip system. Therefore, we interpreted the development of CPO in sheared partially rocks in terms of the following processes.

1. At low strains ($\gamma \lesssim 1$) before melt-enriched regions are well-developed (King et al., 2010), the sense of shear locally within a sample is the same as the applied deformation. The weak CPO reflects a competition between a SPO-induced CPO and a dislocation-glide-produced CPO. The SPO-induced contribution to CPO develops somewhat more slowly with increasing strain than does the dislocation-glide-produced contribution, resulting in a very weak A-type fabric, as illustrated schematically in Figure 14a. The fabric observed in radial section I in Figure 4 is at this stage.
2. At somewhat larger strains ($1 \lesssim \gamma \lesssim 4$), melt segregation results in the formation of melt-enriched regions, such that the CPO reflects strain partitioning between melt-enriched and melt-depleted regions with the local sense of shear rotated ~20° counterclockwise from the bulk shear direction, as indicated schematically in Figure 14b. The fabrics observed in tangential section in Figure 6a with $\gamma \approx 2.4$ and in radial section II in Figure 4 are at this stage.
3. At still larger strain, the contribution of shape-controlled rotation to the CPO overtakes the contribution of lattice rotation due to dislocation glide. As a result, the CPO transitions from one with a weak alignment of [100] axes in the shear direction to one with a weak alignment of [001] axes in the shear direction. A combination of shape-controlled rotation and dislocation glide, therefore, results in the a-c girdle, characteristic of the a-c switch, as illustrated schematically in Figure 14c. The fabrics in tangential sections in Figure 6a with $\gamma \geq 7$ and radial sections III–VI are at this final stage.

In summary, our model incorporates deformation dominated by the easy slip system, (010)[100], and the rotation of crystallographically controlled lentil-shaped olivine grains with long along [001] axes and short along [010]. In the next two subsections, we will discuss the evidence for these two processes.

4.2. Dislocation Activity

The stress exponent of $n = 2.1$–2.4 determined for our samples of olivine + basaltic melt in Figure 3 suggests a significant contribution from dislocations to deformation (e.g., Kohlstedt & Hansen, 2015).

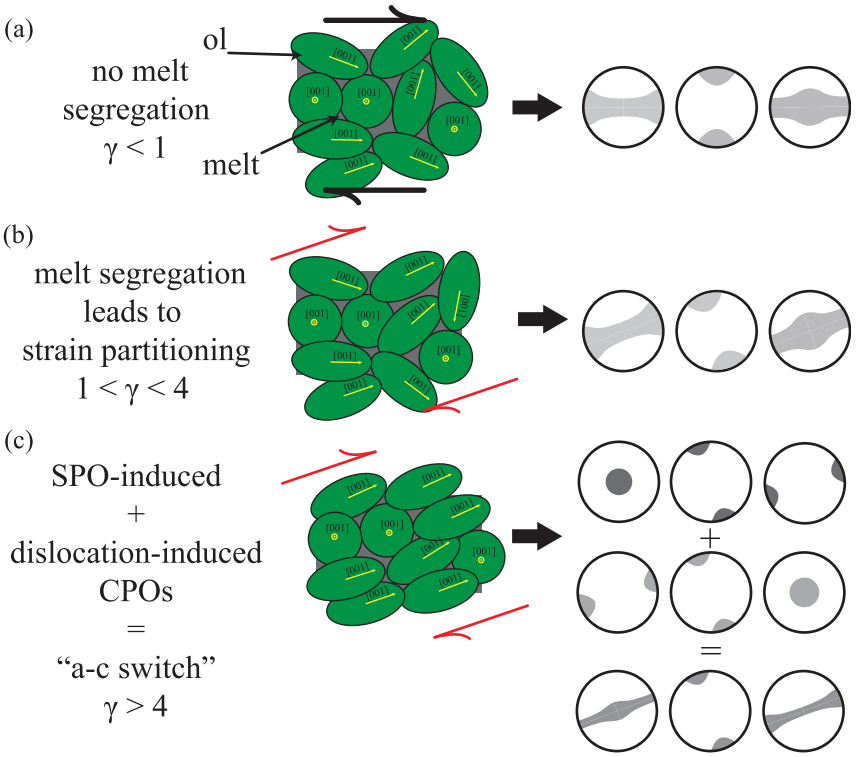

Figure 14. Schematic drawings for the development of CPO viewed in tangential sections. The local sense of shear is indicated by different arrows in each panel. Grain shape change due to deformation is neglected. The projections of elongated grains in a tangential section will have various shapes, but to be simple, circles represent grains with [001] axes normal to the tangential surface and ellipses represent grains with other [001] axes orientations, as illustrated by the yellow lines. The light gray for the pole figures in Figure 14c suggests the crystallographic fabric is weak.

Furthermore, based on the marked dependence of creep rate on grain size for partially molten rocks deformed under similar conditions (Hansen et al., 2011; Hirth & Kohlstedt, 1995; Wang et al., 2010), we conclude that the samples in this study were deformed in the dislocation-accommodated GBS regime.

The inverse pole figures for misorientation axes in Figures 6a and 6b demonstrate that there are significant distortions within grains that are induced by dislocations. In Figure 10, the high density of geometrically necessary dislocations demonstrates the important role of glide to deformation in our samples. The plots of misorientation axes offer a pragmatic approach for analyzing subgrain structure for large quantities of data, whereas the GND map provides a more precise and quantitative analysis of a larger fraction of the substructure within a more limited area. Both approaches demonstrate significant dislocation activity in our deformed samples.

4.3. Crystal Habit of Olivine

Studies of the morphology of olivine grains in an ultramafic melt demonstrate a crystal habit with elongation along the [001] axis and flattening parallel to the (010) plane [e.g., Donaldson, 1976; Drever & Johnston, 1958; Fleet, 1975; t'Hart, 1978). As demonstrated in Figure 11, grains in our samples exhibit a similar morphology.

We note that in a recent study, Miyazaki et al. (2013) argued for a SPO-induced CPO for a forsterite + diopside rock deformed in the diffusion creep regime. In their case, the crystal habit of forsterite exhibited elongation along [100] axis, which resulted in a CPO with [100] axes correspondingly aligned. Since in our experiments, samples were made from San Carlos olivine and basaltic melt, these compositional differences must lead to differences in the crystal habit, yielding an elongation along the [100] axis in one case and along the [001] axis in another case.

4.4. Comparison With a Previously Reported CPO

In Zimmerman et al. [(1999]) reported the CPO for a sample of olivine +∼4% MORB (sample number PT0273) deformed in direct shear at 1,523 K and 300 MPa to a shear strain of 3. Based on a small dataset obtained using a universal stage, these authors reported an A-type fabric with [100] aligned parallel to the shear direction and [010] normal to the shear plane. The CPO for this sample was subsequently reanalyzed with a significantly larger dataset obtained at much higher spatial resolution using EBSD measurements, as presented in Figure 2a by Holtzman et al. (2003a); this sample is identified in Table S1 of their supporting information as sample 273. The newly determined CPO is characterized by a [100]–[001] girdle in the shear plane with [100] weakly aligned normal to the shear direction, much as observed in our samples deformed in torsion. The [010] axes, however, are not back rotated because melt-rich bands did not form in this sample. Thus, the CPO of this partially molten sample deformed in direct shear is fully consistent with the CPO determined for our samples deformed in torsion.

4.5. Other Possible Explanations for the a-c Switch

As outlined in the section 1, two other models have been proposed for the a-c switch. First, the null hypothesis states that not only the (010)[100] but also the (010)[001] slip system contributed to deformation in partially molten olivine-rich rocks, even though (010)[100] dominates in melt-free olivine aggregates. Results from deformation experiments on olivine single crystals demonstrating that deformation on the (010)[001] slip system is orders of magnitude slower than deformation on the (010)[100] slip system rule out this hypothesis.

Second, the hypothesis proposed by Holtzman et al. (2003a) based on anisotropic partitioning of deformation between dislocation and diffusion mechanisms based on stress-induced anisotropic distribution of melt is more difficult to dismiss. Possibly the strongest argument in favor of the model developed in this paper relates to the evolution of CPO with increasing strain. Shear experiments on melt-bearing samples reveal a fabric with [100] axes weakly aligned in the shear direction and [010] axes normal to the shear plane at low strains, as anticipated for glide on (010)[100]. With increasing strain, [001] axes become weakly aligned in the shear direction with [010] becoming more strongly aligned normal to the shear plane, consistent with rotation of olivine grains with a crystallographically controlled SPO superimposed on the fabric formed by glide on (010)[100]. If grain shape-controlled rotation and dislocation glide operate simultaneously, this evolution is not surprising because the contribution of grain shape-controlled rotation to CPO is expected to lag that from dislocation glide, since the latter contributes to the development of a relatively strong CPO even at very low strain in melt-free samples (Hansen et al., 2014). In contrast, anisotropic partitioning of strain between deformation mechanisms should take place even at low strains because alignment of melt pockets responds quickly to the application of a nonhydrostatic stress. Thus, the observed evolution of CPO with increasing strain is more difficult to explain based on anisotropy in contributions for diffusion and dislocation processes.

4.6. Applicability to Nature

Because melt structures are rarely frozen in and directly observable in mantle rocks, it is difficult to prove that a given CPO results from deformation in a partially molten state. However, one of the more common olivine CPOs is very similar to the girdled CPO presented in this study. Questions on the inference of the process that form natural CPOs are presented below.

1. *Is the a-c switch observed in natural rocks?* The classic olivine fabric database of Isma il and Mainprice (1998) presented an olivine CPO with girdles in [100] and [001] axes as one of the third most common (10.1% in the database, Mainprice, 2007), comprising xenoliths and peridotite massif samples from a range of geodynamic settings. In this fabric type, the foliation is often relatively clear, but the lineation may be more subtle, so it can be difficult to infer shear direction and therefore the relation of [100] and [001] axes (and weak concentrations of them in the girdle) to that shear direction. Therefore, we do not expect a great deal of direct evidence, but consider the AG-fabric to be a good indication of the possibility of the a-c switch in nature. The CPO of olivine with girdles of [100] and [001] axes and clusters of [010] axes has been reported to be the second-most common occurrence of all olivine fabrics in western Pacific convergence region (Michibayashi et al., 2016). A similar girdled olivine CPO was observed in mantle xenoliths from the Ontong Java Plateau mantle root (Tommasi & Ishikawa, 2014). An olivine CPO very similar to that associated with the a-c switch was also reported in a plagioclase-bearing peridotite

from the northwestern part of the central Lanzo massif, where evidence exists for melt presence during deformation (Higgie & Tommasi, 2014). Moreover, Drouin et al. (2010) reported a weak fabric with [001] slightly concentrated in the shear direction in natural olivine-rich troctolites, which they interpret as resulting from a pre-existing A-type fabric that was modified by the rotation of elongated grains around [001] axes during melt impregnation.

2. *Is there any evidence of a SPO-induced CPO in nature?* A SPO and a CPO with a [001] maximum aligned subparallel to the shear direction were reported in both experimentally sheared amphibole (Getsinger & Hirth, 2014) and amphibolite-grade natural shear zones (Getsinger et al., 2013). These authors took the correlation of the SPO and CPO as the evidence of a SPO-induced CPO formed during diffusion creep.
3. *How does deformation mechanism affect the CPO?* We cannot know how to extrapolate fabric transitions from experimental to natural conditions without knowing what mechanisms are at play and their relative kinetics. Our samples were deformed in dislocation-accommodated GBS regime, so both dislocation activity and grain rotation happen, which is essential for our model. As argued by Maruyama and Hiraga (2017a, 2017b), GBS facilitates grain rotation producing a SPO-induced CPO. Based on our model, we provide a simple speculation for a partially molten rock. Under our experimental temperature and confining pressure, if deformed in the dislocation creep regime, olivine is expected to exhibit a dislocation-induced CPO with [100] axes clustering parallel to the shear direction (A-type fabric); if deformed in the diffusion creep regime, olivine is expected to exhibit a SPO-induced CPO with [001] axes clustering parallel to the shear direction (B-type fabric). Speculatively, any scaling approach would balance the rotation rate of oblong grains with the rate of dynamic recrystallization. The rotation rate, which may be a function of aspect ratio and possibly grain size, is rate-limited by the dominant mechanism for GBS.
4. *Is melt segregation necessary in this model?* As we discuss in section 4.1.2, melt segregation changes the local shear direction, which results in the counterclockwise rotation of the fabric relative to the applied bulk shear direction. Based on the CPO reported in Holtzman et al. (2003a, Figure 2a), in regions of mantle where melt segregation does not occur, our model predicts a CPO with girdled [100] and [001] axes and clustered [010] axes, that is, the a-c switch without the counterclockwise rotation.
5. *How does melt fraction affect the CPO?* The presence of melt causes a crystallographically controlled grain shape and facilitates grain rotation. As melt fraction decreases, these two functions of melt would become less effective. Further experiments are needed to determine the lower limit of the melt fraction that results in the a-c switch.
6. *What is the significance of the a-c switch, if it exists in the Earth?* Our observations suggest a different evolution of seismic anisotropy from melt-free samples, not just in the magnitude or orientation, but also in the rate of development of anisotropy, which will impact interpretations of upper mantle flow. The seismic anisotropy predicted by the direct application of the results from microstructural analyses of our deformed melt-bearing samples has been presented in Hansen et al. (2016, Figure 2). Specifically, values of azimuthal anisotropy lie $>60^\circ$, typically about 90°, to the shear direction, radial anisotropy exhibits low values, $\sim$1.03, compared to values for melt-free olivine, $\sim$1.06, and such anisotropy becomes evident and stable at a strain as low as 2. When considering natural heterogeneity, the predicted anisotropy may be well approximated as transverse isotropic, which would explain many measurements of upper mantle anisotropy (Hansen et al., 2016; Holtzman & Kendall, 2010; Kawakatsu et al., 2009).

We envision that the a-c switch could provide an alternative explanation for the seismic anisotropy observed in regions where partial melting occurs. At subduction zones, for example, a trench/fault-parallel polarization of seismic waves has been reported (e.g., Barak & Klemperer, 2016; Smith et al., 2001; Wei et al., 2016). This observation has been interpreted as a trench-parallel mantle flow (Smith et al., 2001) or an alignment of melt pockets (Barak & Klemperer, 2016). Building on the proposal of Holtzman et al. (2003a), the a-c switch could explain the trench-parallel fast directions observed in oblique subduction zones. This explanation relies simply on the effect of melt on CPO without calling upon the elastic effects of aligned melt at the grain scale or larger (e.g., Holtzman & Kendall, 2010), trench-parallel flow (e.g., Hall et al., 2000; Kneller & Van Keken, 2007; Smith et al., 2001), high stress and water content (Jung & Karato, 2001), or 3-D flow (Mehl et al., 2003). Beneath the mid-ocean ridges, where partial melting also occurs, a $\sim10^\circ$ misalignment between the azimuth of seismic anisotropy and the plate-spreading direction has been interpreted as a skew between the mantle-divergence and plate-spreading directions based on the seismic anisotropy

induced by olivine A-type fabric (e.g., Toomey et al., 2007; VanderBeek et al., 2016). This $\sim 10^{\circ}$ misalignment may potentially be attributed to a $\sim 10^{\circ}$ azimuthal anisotropy to the shear direction produced in a region composed of mixed melt-bearing and melt-free layers sheared to low strains ($\gamma \leq 5$), as exhibited in Figure 2 in *Hansen et al.* (2016).

5. Conclusions

In this study, we investigated the evolution of the CPO in partially molten rocks deformed under torsion. Here we first summarize the observations and then the implications.

1. The a-c switch becomes evident at $r > 2.2$ mm (corresponding to $\gamma > 4$) in a radial section and at $\gamma > 4$ in a strain series.
2. The CPOs in our partially molten samples are very weak compared to the CPOs in melt-free olivine deformed at similar stresses to similar strains and exhibit little change with increasing stress or strain. This observation implies that two different CPO-formation mechanisms are competing with each other during the entire deformation process.
3. Misorientation axes of subgrain boundaries tend to be aligned with [001] axes and, to a lesser extent, with [010] axes, indicating (010)[100] being the dominant slip system and thus the a-c switch is not caused by (010)[001] being the dominant slip system.
4. Maps of GND density reveal that (010)[100] edge dislocations are the most abundant dislocation type and contribute to nearly all of the visible substructures. This observation implies that dislocation glide on (010)[100] slip system contributes to the CPO formation.
5. Olivine grain shape is crystallographically controlled with elongation along [001] axes and flattening parallel to (010) planes in olivine + basaltic melt samples.
6. A strong correlation exists between the modal orientation of [001] axes and the SPO. This observation implies that the SPO could induce the observed CPO.

Thus, for partially molten samples, we interpret the development of the CPO characterized by girdled [100] and [001] axes in the slip plane in terms of two competing mechanisms: (i) A crystallographically controlled SPO-induced CPO leading to a clustering of [001] axes parallel to the shear direction with [100] axes in the shear plane normal to the shear direction, and (ii) dislocation glide on the (010)[100] slip system, leading to a clustering of [100] axes parallel to the shear direction with [001] axes in the shear plane normal to shear direction. This competition results in a weak concentration of shear-normal [100] axes. This model has important implications for interpreting the flow field from seismic anisotropy in partially molten regions of Earth's mantle.

Acknowledgments
This work benefited greatly from stimulating discussions with Takehiko Hiraga. We thank to Jessica Warren for inspiring discussions, the use of SEM and EBSD facilities at the Department of Plant Biology in Carnegie Institution of Stanford University, and the use of EBSD data processing software. We are also grateful to Yan Liang and Clint Conrad for providing the alkali basalt, to Mark Zimmerman for his help with this work, and to Matěj Peč and Cameron Meyers for their help with collecting EBSD data. Discussions with Max Bezada and Joseph Byrnes are appreciated. We appreciate the constructive comments from Shunichiro Karato, Holger Stünitz and an anonymous reviewer. This work was supported by NSF grants OCE-1459717 and EAR-1520647 to DLK and NERC grant NE/M000966/1 to LNH. Data presented in this paper are accessible via the data repository for the University of Minnesota (http://hdl.handle.net/11299/192485).

References

Bachmann, F., Hielscher, R., & Schaeben, H. (2010). Texture analysis with MTEX—Free and open source software toolbox. *Solid State Phenomena*, *160*, 63–68.
Bai, Q., Mackwell, S. J., & Kohlstedt, D. L. (1991). High-temperature creep of olivine single crystals. 1: Mechanical results for buffered samples. *Journal of Geophysical Research*, *96*(B2), 2441–2463.
Barak, S., & Klemperer, S. L. (2016). Rapid variation in upper-mantle rheology across the San Andreas fault system and Salton trough, southernmost California, USA. *Geology*, *44*(7), 575–578.
Bunge, H. J. (1982). *Texture analysis in materials science: Mathematical methods*. London, UK: Butterworths.
Bussod, G. Y., & Christi, J. M. (1991). Textural development and melt topology in spinel lherzolite experimentally deformed at hypersolidus conditions. *Journal of Petrology*, *Special_Volume*(2), 17.
Bystricky, M., Heidelbach, F., & Mackwell, S. (2006). Large-strain deformation and strain partitioning in polyphase rocks: Dislocation creep of olivine-magnesiowüstite aggregates. *Tectonophysics*, *427*(1–4), 115–132.
Cooper, R. F., & Kohlstedt, D. L. (1984). Solution-precipitation enhanced diffusional creep of partially molten olivine-basalt aggregates during hot-pressing. *Tectonophysics*, *107*(3–4), 207–233.
Cooper, R. F., & Kohlstedt, D. L. (1986). Rheology and structure of olivine-basalt partial melts. *Journal of Geophysical Research*, *91*(B9), 9315–9323.
Couvy, H., Frost, D. J., Heidelbach, F., Nyilas, K., Ungar, T., Mackwell, S., & Cordier, P. (2004). Shear deformation experiments of forsterite at 11 gpa-1400 c in the multianvil apparatus. *European Journal of Mineralogy*, *16*(6), 877–889.
Daines, M., & Kohlstedt, D. (1997). Influence of deformation on melt topology in peridotites. *Journal of Geophysical Research*, *102*(B5), 10257–10210,271.
de Bresser, J., Ter Heege, J., & Spiers, C. (2001). Grain size reduction by dynamic recrystallization: Can it result in major rheological weakening? *International Journal of Earth Sciences*, *90*(1), 28–45.
Donaldson, C. H. (1976). An experimental investigation of olivine morphology. *Contributions to Mineralogy and Petrology*, *57*(2), 187–213.
Drever, H. I., & Johnston, R. (1958). Xiii. Crystal growth of forsteritic olivine in magmas and melts, *Earth and Environmental Science*. *Transactions of the Royal Society of Edinburgh*, *63*(2), 289–315.

Drouin, M., Ildefonse, B., & Godard, M. (2010). A microstructural imprint of melt impregnation in slow spreading lithosphere: Olivine-rich troctolites from the Atlantis massif, Mid-Atlantic ridge, 30 n, iodp hole u1309d. *Geochemistry, Geophysics, Geosystems*, *11*, Q06003. https://doi.org/10.1029/2009GC002995

Durham, W. B., & Goetze, C. (1977). Plastic flow of oriented single crystals of olivine: 1. Mechanical data. *Journal of Geophysical Research*, *82*(36), 5737–5753.

Fleet, M. E. (1975). The growth habits of olivine - a structural interpretation. *Canadian Mineralogist*, *13*, 293–297.

Getsinger, A., & Hirth, G. (2014). Amphibole fabric formation during diffusion creep and the rheology of shear zones. *Geology*, *42*(6), 535–538.

Getsinger, A., Hirth, G., Stünitz, H., & Goergen, E. (2013). Influence of water on rheology and strain localization in the lower continental crust. *Geochemistry, Geophysics, Geosystems*, *14*, 2247–2264. https://doi.org/10.1002/ggge.20148

Ghosh, S. K., & Ramberg, H. (1976). Reorientation of inclusions by combination of pure shear and simple shear. *Tectonophysics*, *34*(1–2), 1–70.

Hall, C. E., Fischer, K. M., Parmentier, E. M., & Blackman, D. K. (2000). The influence of plate motions on three-dimensional back arc mantle flow and shear wave splitting. *Journal of Geophysical Research*, *105*(B12), 28009–28033.

Hansen, L. N., Qi, C., & Warren, J. M. (2016). Olivine anisotropy suggests Gutenberg discontinuity is not the base of the lithosphere, *Proceedings of the National Academy of Sciences of United States of America*, *113*(38), 10503–10506.

Hansen, L. N., Zhao, Y.-H., Zimmerman, M. E., & Kohlstedt, D. L. (2014). Protracted fabric evolution in olivine: Implications for the relationship among strain, crystallographic fabric, and seismic anisotropy. *Earth and Planetary Science Letters*, *387*, 157–168.

Hansen, L. N., Zimmerman, M. E., & Kohlstedt, D. L. (2011). Grain boundary sliding in San Carlos olivine: Flow law parameters and crystallographic-preferred orientation. *Journal of Geophysical Research*, *116*, B08201. https://doi.org/10.1029/2011JB008220

Higgie, K., & Tommasi, A. (2014). Deformation in a partially molten mantle: Constraints from plagioclase lherzolites from Lanzo, Western Alps. *Tectonophysics*, *615-616*, 167–181.

Hildyard, R. C., Prior, D. J., Faulkner, D. R., & Mariani, E. (2009). Microstructural analysis of anhydrite rocks from the Triassic evaporites, Umbria-Marche Apennines, Central Italy: An insight into deformation mechanisms and possible slip systems. *Journal of Structural Geology*, *31*(1), 92–103.

Hirth, G., & Kohlstedt, D. (2003). Rheology of the upper mantle and the mantle wedge: A view from the experimentalists. In J. Eiler (Ed.), *Inside the subduction factory* (pp. p 83–105). Washington, DC: AGU. https://doi.org/10.1029/138GM06

Hirth, G., & Kohlstedt, D. L. (1995). Experimental constraints on the dynamics of the partially molten upper mantle: 2. Deformation in the dislocation creep regime. *Journal of Geophysical Research 100*(B8), 15441–15449.

Holtzman, B. K., Groebner, N. J., Zimmerman, M. E., Ginsberg, S. B., & Kohlstedt, D. L. (2003b). Stress-driven melt segregation in partially molten rocks. *Geochemistry Geophysics Geosystems*, *4*(5), 8607. https://doi.org/10.1029/2001GC000258

Holtzman, B. K., & Kendall, J.-M. (2010). Organized melt, seismic anisotropy, and plate boundary lubrication. *Geochemistry, Geophysics, Geosystems*, *11*, Q0AB06. https://doi.org/10.1029/2010GC003296

Holtzman, B. K., Kohlstedt, D. L., & Morgan, J. P. (2005). Viscous energy dissipation and strain partitioning in partially molten rocks. *Journal of Petrology*, *46*(12), 2569–2592.

Holtzman, B. K., Kohlstedt, D. L., Zimmerman, M. E., Heidelbach, F., Hiraga, T., & Hustoft, J. (2003). Melt segregation and strain partitioning: Implications for seismic anisotropy and mantle flow. *Science*, *301*(5637), 1227.

Ildefonse, B., Launeau, P., Bouchez, J.-L., & Fernandez, A. (1992a). Effect of mechanical interactions on the development of shape preferred orientations: A two-dimensional experimental approach. *Journal of Structural Geology*, *14*(1), 73–83.

Ildefonse, B., Sokoutis, D., & Mancktelow, N. S. (1992b). Mechanical interactions between rigid particles in a deforming ductile matrix: Analogue experiments in simple shear flow. *Journal of Structural Geology*, *14*(10), 1253–1266.

Isma Il, W. B., & Mainprice, D. (1998). An olivine fabric database: An overview of upper mantle fabrics and seismic anisotropy. *Tectonophysics*, *296*(1), 145–157.

Jiang, J., Britton, T., & Wilkinson, A. (2013). Measurement of geometrically necessary dislocation density with high resolution electron backscatter diffraction: Effects of detector binning and step size. *Ultramicroscopy*, *125*, 1–9.

Jung, H., & Karato, S-I. (2001). Water-induced fabric transitions in olivine. *Science*, *293*(5534), 1460–1463.

Katz, R. F., & Takei, Y. (2013). Consequences of viscous anisotropy in a deforming, two-phase aggregate. Part 2: Numerical solutions of the full equations. *Journal of Fluid Mechanics*, *734*, 456–485.

Kawakatsu, H., Kumar, P., Takei, Y., Shinohara, M., Kanazawa, T., Araki, E., et al. (2009). Seismic evidence for sharp lithosphere-asthenosphere boundaries of oceanic plates. *Science*, *324*(5926), 499–502.

King, D. S., Zimmerman, M. E., & Kohlstedt, D. L. (2010). Stress-driven melt segregation in partially molten olivine-rich rocks deformed in torsion. *Journal of Petrology*, *51*(1–2), 21–42.

Kneller, E. A., & Van Keken, P. E. (2007). Trench-parallel flow and seismic anisotropy in the Mariana and Andean subduction systems. *Nature*, *450*(7173), 1222–1225.

Kohlstedt, D. L., & Hansen, L. N. (2015). Constitutive equations, rheological behavior, and viscosity of rocks. In G. Schubert (Ed.), *Treatise on geophysics*. (2nd ed., pp. 441–472). Oxford, UK: Elsevier.

Kohlstedt, D. L., & Holtzman, B. K. (2009). Shearing melt out of the earth: An experimentalist's perspective on the influence of deformation on melt extraction. *Annual Review of Earth and Planetary Sciences*, *37*(1), 561–593.

Kohlstedt, D. L., & Zimmerman, M. E. (1996). Rheology of partially molten mantle rocks. *Annual Review of Earth and Planetary Sciences*, *24*(1), 41–62.

Lloyd, G. E., Farmer, A. B., & Mainprice, D. (1997). Misorientation analysis and the formation and orientation of subgrain and grain boundaries. *Tectonophysics*, *279*(1–4), 55–78.

Mainprice, D. (2007). Seismic anisotropy of the deep earth from a mineral and rock physics perspective. In G. Schubert (Ed.), *Treatise on geophysics* (Vol. 2, pp. 441–472). Oxford, UK: Elsevier.

Maruyama, G., & Hiraga, T. (2017a). Grain-to multiple-grain-scale deformation processes during diffusion creep of forsterite + diopside aggregate. 1: Direct observations. *Journal of Geophysical Research: Solid Earth*, *122*, 5890–5915. https://doi.org/10.1002/2017JB014254

Maruyama, G., & Hiraga, T. (2017b). Grain-to multiple-grain-scale deformation processes during diffusion creep of forsterite + diopside aggregate. 2: Grain-boundary-sliding induced grain rotation and its role in crystallographic preferred orientation in rocks. *Journal of Geophysical Research: Solid Earth*, *122*, 5916–5934. https://doi.org/10.1002/2017JB014255

Mehl, L., Hacker, B. R., Hirth, G., & Kelemen, P. B. (2003). Arc-parallel flow within the mantle wedge: Evidence from the accreted Talkeetna arc, south central Alaska. *Journal of Geophysical Research*, *108*(B8), 2375. https://doi.org/10.1029/2002JB002233

Michibayashi, K., Mainprice, D., Fujii, A., Uehara, S., Shinkai, Y., Kondo, Y., et al. (2016). Natural olivine crystal-fabrics in the western pacific convergence region: A new method to identify fabric type. *Earth and Planetary Science Letters*, *443*, 70–80.

Miyazaki, T., Sueyoshi, K., & Hiraga, T. (2013). Olivine crystals align during diffusion creep of earth/'s upper mantle. *Nature*, *502*(7471), 321–326.
Morgan, Z., & Liang, Y. (2003). An experimental and numerical study of the kinetics of harzburgite reactive dissolution with applications to dunite dike formation. *Earth and Planetary Science Letters*, *214*(1–2), 59–74.
Ohuchi, T., Kawazoe, T., Nishihara, Y., Nishiyama, N., & Irifune, T. (2011). High pressure and temperature fabric transitions in olivine and variations in upper mantle seismic anisotropy. *Earth and Planetary Science Letters*, *304*(1–2), 55–63.
Paterson, M. S., & Olgaard, D. L. (2000). Rock deformation tests to large shear strains in torsion. *Journal of Structural Geology*, *22*(9), 1341–1358.
Phakey, P., Dollinger, G., & Christie, J. (1972). Transmission electron microscopy of experimentally deformed olivine crystals. In H. C. Heard et al. (Eds.), *Flow and fracture of rocks* (pp. 117–138). Washington, DC: AGU. https://doi.org/10.1029/GM016p0117
Prior, D. J., Wheeler, J., Peruzzo, L., Spiess, R., & Storey, C. (2002). Some garnet microstructures: An illustration of the potential of orientation maps and misorientation analysis in microstructural studies. *Journal of Structural Geology*, *24*(6–7), 999–1011.
Qi, C., Kohlstedt, D. L., Katz, R. F., & Takei, Y. (2015). Experimental test of the viscous anisotropy hypothesis for partially molten rocks. *Proceedings of the National Academy of Sciences of United States of America*, *112*(41), 12616–12620.
Qi, C., Zhao, Y.-H., & Kohlstedt, D. L. (2013). An experimental study of pressure shadows in partially molten rocks. *Earth and Planetary Science Letters*, *382*, 77–84.
Raterron, P., Amiguet, E., Chen, J., Li, L., & Cordier, P. (2009). Experimental deformation of olivine single crystals at mantle pressures and temperatures. *Physics of the Earth and Planetary Interiors*, *172*(1–2), 74–83.
Ricoult, D. L., & Kohlstedt, D. L. (1985). Experimental evidence for the effect of chemical environment upon the creep rate of olivine. In R. N. Schock (Ed.), *Point defects in minerals, Geophys. Monogr. Ser.* (Vol. 31, pp. 171–184), Washington, DC: AGU.
Schwindinger, K. R., & Anderson, A. T. Jr (1989). Synneusis of kilauea iki olivines. *Contributions to Mineralogy and Petrology*, *103*(2), 187–198.
Skemer, P., Katayama, I., Jiang, Z., & Karato, S-I. (2005). The misorientation index: Development of a new method for calculating the strength of lattice-preferred orientation. *Tectonophysics*, *411*(1–4), 157–167.
Smith, G. P., Wiens, D. A., Fischer, K. M., Dorman, L. M., Webb, S. C., & Hildebrand, J. A. (2001). A complex pattern of mantle flow in the Lau Backarc. *Science*, *292*(5517), 713–716.
Takei, Y. (2001). Stress-induced anisotropy of partially molten media inferred from experimental deformation of a simple binary system under acoustic monitoring. *Journal of Geophysical Research*, *106*(B1), 567–588.
Takei, Y., & Holtzman, B. K. (2009). Viscous constitutive relations of solid-liquid composites in terms of grain boundary contiguity: 3. Causes and consequences of viscous anisotropy. *Journal of Geophysical Research*, *114*, B06207. https://doi.org/10.1029/2008JB005850
Takei, Y., & Katz, R. F. (2013). Consequences of viscous anisotropy in a deforming, two-phase aggregate. Part 1: Governing equations and linearized analysis. *Journal of Fluid Mechanics*, *734*, 424–455.
t'Hart, J. (1978). The structural morphology of olivine. ii: A quantitative derivation. *Canadian Mineralogist*, *16*, 547–560.
Tielke, J. A., Hansen, L. N., Tasaka, M., Meyers, C., Zimmerman, M. E., & Kohlstedt, D. L. (2016). Observations of grain size sensitive power law creep of olivine aggregates over a large range of lattice-preferred orientation strength. *Journal of Geophysical Research: Solid Earth*, *121*, 506–516. https://doi.org/10.1002/2015JB012302
Tommasi, A., & Ishikawa, A. (2014). Microstructures, composition, and seismic properties of the Ontong java plateau mantle root. *Geochemistry, Geophysics, Geosystems*, *15*, 4547–4569. https://doi.org/10.1002/2014GC005452
Toomey, D. R., Jousselin, D., Dunn, R. A., Wilcock, W. S. D., & Detrick, R. S. (2007). Skew of mantle upwelling beneath the east pacific rise governs segmentation. *Nature*, *446*(7134), 409–414.
VanderBeek, B. P., Toomey, D. R., Hooft, E. E. E., & Wilcock, W. S. D. (2016). Segmentation of mid-ocean ridges attributed to oblique mantle divergence. *Nature Geoscience*, *9*(8), 636–642.
Wallis, D., Hansen, L. N., Britton, T. B., & Wilkinson, A. J. (2016). Geometrically necessary dislocation densities in olivine obtained using high-angular resolution electron backscatter diffraction. *Ultramicroscopy*, *168*, 34–45.
Wallis, D., Hansen, L., Ben Britton, N. T., & Wilkinson, A. J. (2017). Dislocation interactions in olivine revealed by HR-EBSD. *Journal of Geophysical Research: Solid Earth*, *122*, 7659–7678. https://doi.org/10.1002/2017JB014513
Wang, Z., Zhao, Y.-H., & Kohlstedt, D. L. (2010). Dislocation creep accommodated by grain boundary sliding in dunite. *Journal of Earth Science*, *21*(5), 541–554.
Wei, S. S., Zha, Y., Shen, W., Wiens, D. A., Conder, J. A., & Webb, S. C. (2016). Upper mantle structure of the Tonga-Lau-Fiji region from Rayleigh wave tomography. *Geochemistry, Geophysics, Geosystems*, *17*, 4705–4724. https://doi.org/10.1002/2016GC006656
Wheeler, J., Mariani, E., Piazolo, S., Prior, D. J., Trimby, P., & Drury, M. R. (2009). The weighted burgers vector: A new quantity for constraining dislocation densities and types using electron backscatter diffraction on 2d sections through crystalline materials. *Journal of Microscopy*, *233*(3), 482–494.
Wilkinson, A. J., Meaden, G., & Dingley, D. J. (2006). High-resolution elastic strain measurement from electron backscatter diffraction patterns: New levels of sensitivity. *Ultramicroscopy*, *106*(4–5), 307–313.
Woodcock, N. H. (1977). Specification of fabric shapes using an eigenvalue method. *Geological Society of America Bulletin*, *88*(9), 1231–1236.
Zhang, S., & Karato, S-I. (1995). Lattice preferred orientation of olivine aggregates deformed in simple shear. *Nature*, *375*(6534), 774–777.
Zimmerman, M. E., Zhang, S., Kohlstedt, D. L., & Karato, S-I. (1999). Melt distribution in mantle rocks deformed in shear. *Geophysical Research Letters*, *26*(10), 1505–1508.